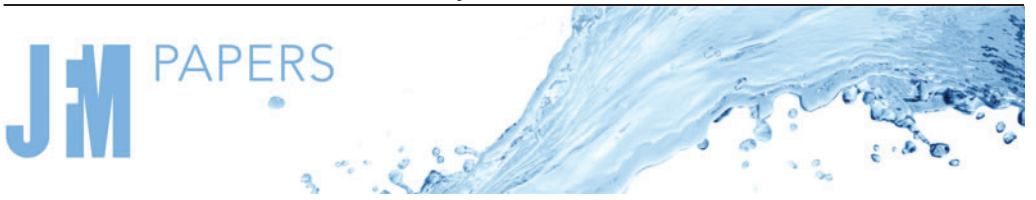
J. Fluid Mech. (2022), *vol*. 948, A12, doi:10.1017/jfm.2022.663



Two-way coupled turbulent particle-laden boundary layer combustion over a flat plate

Guo Chen[1], **Haiou Wang**[1,†], **Kun Luo**[1] **and Jianren Fan**[1]

[1]State Key Laboratory of Clean Energy Utilization, Zhejiang University, Hangzhou 310027, PR China

(Received 1 December 2021; revised 16 June 2022; accepted 28 July 2022)

In the present study, turbulent particle-laden boundary layer combustion over a flat plate is investigated using direct numerical simulation (DNS). A two-way coupled Eulerian–Lagrangian point particle method is used for the solid phase. The effects of particle Stokes numbers, mass loadings and chemical reactions on the interactions between particles and boundary layer turbulence in the near-wall region are explored. It was found that particle heat transfer is dominant over wall heat transfer in the reacting case with heavy particles and large mass loadings, resulting in a lower fluid temperature. Particle accumulation due to the turbophoresis effect in the near-wall region is observed, which is more prominent in the cases with a large Stokes number. The turbophoresis effect is examined via the magnitude of streamwise vorticity Ω_x. It is shown that Ω_x is attenuated by heavy particles, and the attenuation increases with increasing mass loadings. Therefore, particle wall–accumulation is less prominent in the cases with large mass loadings. Compared with the non-reacting cases, the distribution of particles is more inhomogeneous for the reacting cases, where the particles move faster due to intense reactions with increasing wall-normal distance. Finally, the flow topologies and the Reynolds stress anisotropy are examined to understand turbulence modulation by combustion and particles. It was suggested that light particles augment the vortex-dominant topologies, whereas heavy particles have an opposite effect. The anisotropy mapping of the Reynolds stress shows that the flows become more one-dimensional in the near-wall region for the cases with combustion and/or large mass loadings.

Key words: turbulent reacting flows, turbulent boundary layers, particle/fluid flow

1. Introduction

Turbulent wall-bounded combustion laden with particles is widely encountered in industrial combustion devices, including furnaces, rocket engines and aero-engines. The

† Email address for correspondence: wanghaiou@zju.edu.cn

© The Author(s), 2022. Published by Cambridge University Press

https://doi.org/10.1017/jfm.2022.663 Published online by Cambridge University Press

interactions between boundary layer turbulence, combustion, particles and wall are very complex in the near-wall region of practical combustors. For example, turbulence is modulated by combustion (Lipatnikov & Chomiak 2010), and flames are affected by turbulence as well (Driscoll *et al.* 2020). Particle distributions are influenced by coherent turbulence in the boundary layer (Kaftori, Hetsroni & Banerjee 1995; Marchioli & Soldati 2002), and in turn turbulence is also modified by particles (Elghobashi & Truesdell 1993). As the volume of the combustion chamber is limited, flames unavoidably interact with the wall, which may lead to flame quenching and increase pollutant emission (Dreizler & Böhm 2015). Flames have significant effects on quantities such as wall heat flux as well (Poinsot, Haworth & Bruneaux 1993; Gruber *et al.* 2010). Despite its practical importance, existing understanding of turbulent boundary layer combustion laden with particles is insufficient, which motivates the present work.

Numerous studies have reported the particle dispersion and deposition in boundary layer turbulence experimentally (Reeks 1983; Rogers & Eaton 1991; Fessler, Kulick & Eaton 1994; Kaftori *et al.* 1995; Niño & Garcia 1996), numerically (McLaughlin 1989; Pedinotti, Mariotti & Banerjee 1992; Brooke, Hanratty & McLaughlin 1994; Uijttewaal & Oliemans 1996; Li *et al.* 2001; Rouson & Eaton 2001; Marchioli & Soldati 2002; Narayanan *et al.* 2003; Picciotto, Marchioli & Soldati 2005; Picano, Sardina & Casciola 2009; Sardina *et al.* 2012*a*,*b*; Nilsen, Andersson & Zhao 2013; Lee & Lee 2015; Wang *et al.* 2020; Xiao *et al.* 2020) and theoretically (Young & Leeming 1997). These studies mainly focused on (1) preferential concentration and (2) turbophoresis of particles. Preferential concentration is the result of particles being thrown out of the original trajectory by the centrifugal effect, which has been broadly investigated in particle-laden turbulence with or without a wall. In a study of particles in isotropic turbulence, Squires & Eaton (1991) found that particles preferentially concentrate outside the vortical structure. Pedinotti *et al.* (1992) observed that particles tend to accumulate in low-vorticity and high-strain regions in wall-bounded coherent turbulence. Miller & Bellan (1999) showed that liquid particles are preferentially concentrated in high-strain regions of the flow, where the particles have a larger size than those remaining within the vortical structures. Unlike preferential concentration, turbophoresis only occurs in wall-bounded turbulence, which contributes to the wall accumulation of particles and represents the mean drift of the particles towards the wall (Reeks 1983; Young & Leeming 1997; Sardina *et al.* 2012*b*). Despite the above-mentioned studies, there has been no effort devoted to studying the turbophoresis effect in turbulent boundary layer combustion.

A lot of effort has been spent in identifying whether turbulence is enhanced or attenuated by particles (Gore & Crowe 1989; Elghobashi 1994, 2006; Crowe 2000; Kuerten 2016). Elghobashi (1994, 2006) proposed a regime diagram of particle–turbulence interactions to determine whether turbulence is augmented or attenuated by particles as shown in figure 1. It was suggested that when the particle volume fraction is less than 10^{-6}, the effect of the particle on turbulence can be negligible. When the particle volume fraction is between 10^{-6} and 10^{-3}, the particles attenuate turbulent kinetic energy (TKE) if the Stokes number (St_k) is greater than unity and augment TKE if St_k is less than 0.1. When the particle volume fraction is greater than 10^{-3}, particle–particle collisions become important and turbulence is affected by the oscillatory motion induced by particle collisions. A comprehensive review on this topic can be found in Kuerten (2016).

The topic of boundary layer turbulence modulation by particles has also received considerable attention both experimentally (Rashidi, Hetsroni & Banerjee 1990; Rogers & Eaton 1991; Kulick, Fessler & Eaton 1994) and numerically (Pan & Banerjee 1996; Li *et al.* 2001; Portela & Oliemans 2003; Dritselis & Vlachos 2008; Nasr, Ahmadi &

https://doi.org/10.1017/jfm.2022.663 Published online by Cambridge University Press

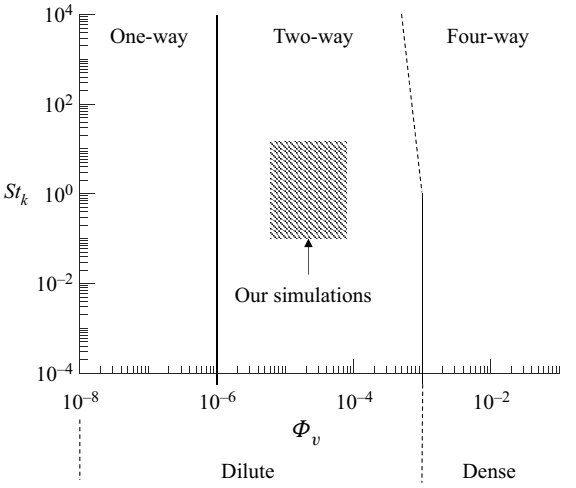


Figure 1. Regime diagram of interactions between particles and turbulence based on Elghobashi (1994) and Elghobashi (2006).

Mclaughlin 2009; Dritselis & Vlachos 2011; Kuerten, van der Geld & Geurts 2011; Zhao, Andersson & Gillissen 2013; Fox 2014; Richter 2015; Capecelatro, Desjardins & Fox 2016; Li, Luo & Fan 2016*a*; Capecelatro, Desjardins & Fox 2018; Wang & Richter 2019; Costa, Brandt & Picano 2020; Zhou *et al.* 2020; Costa, Brandt & Picano 2021). Previous studies investigated the effects of particles on the properties of near-wall turbulence, including turbulent intensity (Rashidi *et al.* 1990; Rogers & Eaton 1991; Li *et al.* 2001; Zhao *et al.* 2013; Li *et al.* 2016*a*), turbulent fluctuation velocity (Kulick *et al.* 1994; Zhao *et al.* 2013), Reynolds stress (Rashidi *et al.* 1990; Pan & Banerjee 1996; Zhao *et al.* 2013; Li *et al.* 2016*a*), coherent quasi-streamwise vortices (Portela & Oliemans 2003; Dritselis & Vlachos 2008, 2011), high- and low-speed streaks (Zhou *et al.* 2020), sweep/ejection events (Rashidi *et al.* 1990; Pan & Banerjee 1996) and TKE (Richter 2015; Capecelatro *et al.* 2016, 2018; Wang & Richter 2019). For particle-laden boundary layer turbulence, controversies exist regarding the effects of particles on the statistics of turbulence in these studies. For instance, some studies (Zhao, Andersson & Gillissen 2010; Zhao *et al.* 2013) found intensity of streamwise turbulence is enhanced by particles, whereas other studies (Kulick *et al.* 1994; Pan & Banerjee 1996; Nasr *et al.* 2009) observed the intensity is attenuated by particles. In addition, Li *et al.* (2001) and Dritselis & Vlachos (2008, 2011) showed that streamwise fluctuating velocity is suppressed in the near-wall region but augmented in the outer region, whereas Li *et al.* (2016*a*) observed a totally opposite trend. Moreover, for small particles with a particle diameter being less than the Kolmogorov length scale, Li *et al.* (2001) and Dritselis & Vlachos (2008) reported that turbulence augmentation increases with increasing inertia, which is in contrast with Kulick *et al.* (1994) and Zhao *et al.* (2013). The above experimental and numerical studies focused on the turbulence modulation by particles near cold walls. Considering that wall-bounded turbulence modulation by solid or liquid particles is widely encountered in practical combustors, it is of significance to explore the modulation of turbulence by particles in boundary layer combustion.

Wall-bounded turbulent combustion has been investigated in the context of gaseous combustion (Poinsot *et al.* 1993; Bruneaux *et al.* 1996; Bruneaux, Poinsot & Ferziger 1997; Alshaalan & Rutland 2002; Wang & Trouvé 2006; Gruber *et al.* 2010; Zhao, Wang

https://doi.org/10.1017/jfm.2022.663 Published online by Cambridge University Press

& Chakraborty 2018; Chen *et al.* 2021; Wang *et al.* 2021*c*,*a*). The wall heat flux is a key quantity to evaluate flame–wall interactions. In a three-dimensional direct numerical simulation (DNS) study of flame–wall interaction in channel flows, Bruneaux *et al.* (1996) observed that coherent turbulence structures push flame elements towards the wall and reduce the quenching distance, which is responsible for the increase of heat flux. This was also analysed theoretically by Poinsot *et al.* (1993). Interestingly, the wall heat flux was also found to be influenced by particles (Kuerten *et al.* 2011; Li, Luo & Fan 2018) in non-reacting flows. Kuerten *et al.* (2011) conducted a DNS study of turbulent particle-laden channel flow, which showed that the wall heat flux is enhanced by large particles with high specific heat capacity. The enhancement is increased with increasing particle mass loadings and specific heat capacity. It was concluded that the turbophoresis effect is responsible for the increase of wall heat flux. Nakhaei & Lessani (2017) performed DNS of a non-isothermal turbulent channel flow laden with inertial particles, and observed that particles with low specific heat capacity lead to attenuation of wall heat flux. Recently, Li *et al.* (2018) investigated particle-laden spatially developing turbulent boundary layer flows over an isothermally heated wall. They found the sweep and ejection events are suppressed by particles, which reduce the temperature fluctuation. Despite these studies of gaseous wall-bounded turbulent combustion and particle-laden non-reacting turbulent boundary layer, there is a dearth of work on particle-laden turbulent boundary layer combustion. As for the studies of interactions between particles and combustion, Picano *et al.* (2011) and Battista *et al.* (2011) conducted experimental and numerical studies of a turbulent Bunsen flame laden with inertial particles, showing that particles are accelerated by flames. However, existing understanding of the interactions between particles, boundary layer turbulence and combustion is still lacking.

In the above context, the present study performs the first DNS of two-way coupled turbulent particle-laden boundary layer combustion and examines the characteristics of heat transfer, particle distribution and turbulence modulation. The remainders of this article are as follows. In § 2, the DNS configuration and numerical methods are briefly introduced. Detailed results are presented and discussed in § 3. Finally, the conclusions are summarised in § 4.

2. DNS configuration and numerical methods

2.1. *DNS configuration*

In the present study, spatially developing turbulent particle-laden boundary layer flows both with and without reactions are considered. The inflow turbulence imposed at the inlet of the main DNS was generated by temporal sampling of an auxiliary simulation of fully developed boundary layer turbulence with a friction Reynolds number being $Re_\tau = 360$, which is defined as

$$Re_\tau = \frac{\rho_w u_\tau \delta}{\mu_w}, \tag{2.1}$$

where $\delta = 7.4\,\text{mm}$ is the boundary layer thickness, ρ_w is the fluid density and μ_w is the fluid viscosity at the wall. The friction velocity u_τ is defined as $u_\tau = \sqrt{\tau_w/\rho_w}$, where τ_w is the wall shear stress. In the main DNS, the free stream velocity is $U_\infty = 100\,\text{m}\,\text{s}^{-1}$, and the temperature is $T_\infty = 1150$ K. The wall is isothermal with a temperature of $T_w = 750\,\text{K}$. The ambient pressure is 1 atm. The composition of the reactant is determined by adiabatic mixing of a H_2/N_2 fuel jet and a vitiated air (i.e. the product of lean natural gas combustion). The equivalence ratio of the inflow mixture is 0.4, and the species mass fractions of O_2, N_2, H_2O and H_2 are 0.1568, 0.7649, 0.0705 and 0.0078, respectively

https://doi.org/10.1017/jfm.2022.663 Published online by Cambridge University Press

Case	St	d_p (μm)	ρ_p (kg m^{-3})	Φ_v	$\Phi_{m,in}$	$N_{p,tot}$
NR1	1.0	4	473	7.55×10^{-5}	0.1	2.5×10^7
NR2	10.0	4	4730	8.15×10^{-6}	0.1	2.7×10^6
NR3	10.0	4	4730	7.85×10^{-5}	1.0	2.6×10^7
R1	1.0	4	473	5.43×10^{-5}	0.1	1.8×10^7
R2	10.0	4	4730	6.04×10^{-6}	0.1	2.0×10^6
R3	10.0	4	4730	6.34×10^{-5}	1.0	2.1×10^7

Table 1. DNS parameters.

(Wang *et al.* 2021*c*, 2020). Under the above-mentioned thermochemical conditions, the inflow mixture is ignitive and the ignition delay time is $\tau_{ig} = 0.11$ ms. The ignition distance calculated as $L_{ig} = \tau_{ig} \times U_\infty$ is 11 mm. No attempt was made to incorporate the effects of radiative heat transfer and surfaces reaction to simplify the physical problems and to focus on the complex interactions between combustion, turbulence and particles near the wall. The complex physics of radiative heat transfer and surface reaction will be considered in future work. Several DNS cases were performed as listed in table 1. The DNS cases without chemical reactions (non-reacting cases) are labelled with 'NR', where the reaction source terms in species mass fraction equations are turned off artificially. The reacting cases are labelled with 'R'.

The size of the computational domain for the main DNS is $L_x \times L_y \times L_z = 60 \times 25 \times 25$ mm^3, where L_x, L_y and L_z correspond to the length in the streamwise, x, wall-normal direction, y, and spanwise direction, z, respectively. Non-reflecting and periodic boundary conditions are applied in the streamwise and spanwise directions, respectively. The boundary condition is no-slip isothermal wall ($y = 0$) and non-reflecting outflow ($y = L_y$) in the wall-normal direction. In the non-reacting cases, the grid of the DNS adequately resolves all turbulent structures. Uniform grids with $\Delta x = 150\,\mu$m and $\Delta z = 130\,\mu$m are used in the streamwise and spanwise directions, respectively. An algebraic stretching grid is used in the wall-normal direction with $\Delta y_{min} = 12\,\mu$m at the wall and gradually stretched outside of this region. The resultant grid number of the non-reacting cases is $N_x \times N_y \times N_z = 400 \times 256 \times 192$. The normalised grid sizes are $\Delta x^+ = 7.1$, $\Delta z^+ = 6.2$ and $\Delta y^+_{min} = 0.6$, where the viscous length scale ($\delta_v = 21\,\mu$m) at the inlet of the DNS is used for the normalisation. There are at least 11 points within $y^+ \leq 10$ to satisfy the wall-normal grid resolution requirement (Moser, Kim & Mansour 1999). The grid resolution is close to those in previous DNS studies (Hetsroni, Mosyak & Pogrebnyak 2002; Zonta, Marchioli & Soldati 2008; Kuerten *et al.* 2011; Nakhaei & Lessani 2017).

The resolution is more demanding in the reacting cases. Therefore, the grid is further refined to resolve the flame. A uniform grid with a resolution of $\Delta x = 62.5\,\mu$m is used in the region of $0 \leq x \leq 20$ mm where the flame locates, and gradually stretched outside of this region. In the wall-normal direction, the grid is stretched from the wall to the outer region with the finest grid of $\Delta y_{min} = 10\,\mu$m at the wall. A uniform grid spacing of $\Delta z = 62.5\,\mu$m is used in the spanwise direction. The resultant grid number of the reacting cases is $N_x \times N_y \times N_z = 800 \times 480 \times 400$. Note that a finer gird resolution was also used for case R1 with a grid number of $N_x \times N_y \times N_z = 1600 \times 480 \times 800$. Figure 2 compares the instantaneous distributions of vorticity magnitude and heat release rate in a typical x–y plane for case R1 without and with grid refinement. As can be seen, the results with these two grid resolutions are very similar.

https://doi.org/10.1017/jfm.2022.663 Published online by Cambridge University Press

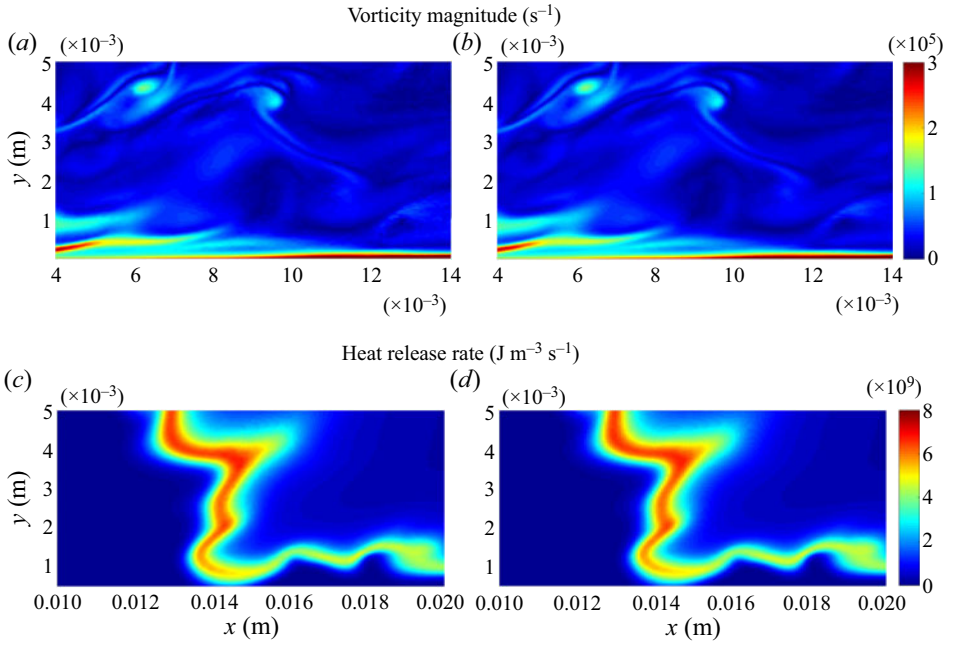


Figure 2. The instantaneous distributions of vorticity magnitude and heat release rate in a typical x–y plane for (a,c) case R1 with a finer grid resolution and (b,d) case R1 with the grid resolution that is used in the present study.

Additional DNS cases without particles were performed to further verify the grid resolution for the flow. Figure 3 shows the mean distributions of van-Driest-transformed streamwise velocity along the wall-normal direction for the non-reacting/reacting cases without particles. The van Driest transformation of streamwise velocity is defined as $u_{VD} = \int (\bar{\rho}/\bar{\rho}_w)^{1/2} \mathrm{d}\bar{u}$. It is observed that the result of the non-reacting DNS is in good agreement with the result of the reference DNS (Schlatter & Örlü 2010). In the reacting case, though u_{VD} is larger in the logarithmic layer due to combustion acceleration, u_{VD} still abides by the law of the wall in the viscous sublayer.

To explore the behaviours of particle dispersion and segregation, cases with different Stokes numbers were performed. In all cases, particles are injected into the domain at the inlet. The initial temperature and velocity for the particles are obtained by interpolating those of the surrounding fluid to the particle position. The parameters for various DNS cases are provided in table 1. Two kinds of particles are considered by changing the particle density to achieve specific Stokes numbers (i.e. $St = 1.0$ and 10.0). Note that the density of light particles is close to that of biomass, whereas the density of heavy particles is close to that of hematite. The particle Stokes number $St = \tau_p/\tau_f$ is based on the particle relaxation timescale $\tau_p = \rho_p d_p^2/(18\mu)$ and the characteristic flow timescale $\tau_f = \delta^*/u_\infty$ (Ganapathisubramani, Clemens & Dolling 2006; Li *et al.* 2016*a*; Wang *et al.* 2020), where δ^* is the momentum thickness of the boundary layer. The base value of the inflow particle mass loading in the DNS is 0.1, which is defined as

$$\Phi_{m,in} = \frac{\rho_p N_{p,in}(y) V_{par}}{\bar{\rho}_{in}(y)\bar{u}_{in}(y)\Delta t \Delta y L_z}, \tag{2.2}$$

https://doi.org/10.1017/jfm.2022.663 Published online by Cambridge University Press

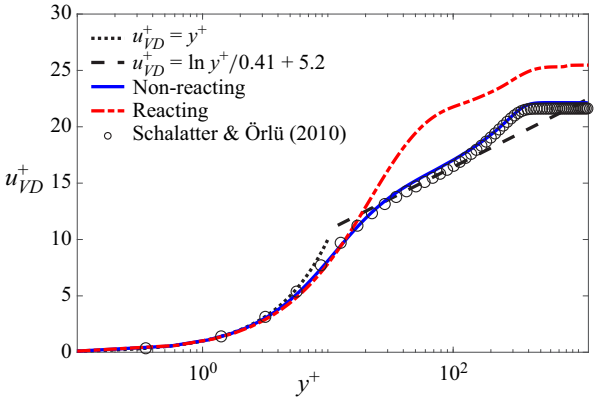


Figure 3. The mean distributions of van-Driest-transformed streamwise velocity of fluid phase along the y^+ for non-reacting/reacting particle-free cases. The black circles denote the result of previous DNS study by Schlatter & Örlü (2010).

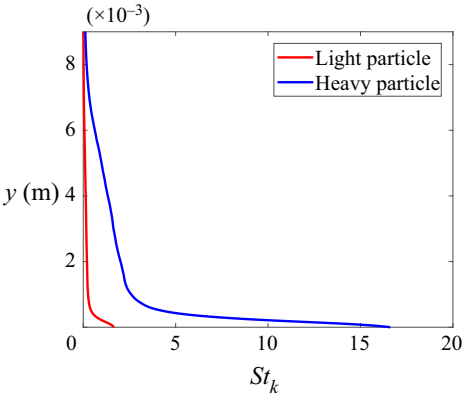


Figure 4. The variations of the Stokes number based on the Kolmogorov timescale.

where $N_{p,in}(y)$ is the number of particles released at the height of y, V_{par} is the volume of a single particle, Δt is the time interval for particle release, Δy is the height of control volume in y direction and $\bar{\rho}_{in}(y)$ and $\bar{u}_{in}(y)$ are the Reynolds-averaged density and velocity of the fluid at the height of y, respectively. To investigate the effects of particle mass loading on the flows, the inflow particle mass loading is increased to 1.0 in cases NR3 and R3.

The overall volume fraction Φ_v is defined as the volume ratio of all particles to the fluid, which is lower in the reacting cases due to the thermal expansion. Combustion accelerates the fluid phase, which drives the acceleration of the solid phase, so the overall volume fraction of particles decreases. It is useful to determine the location of our simulations in the regime diagram of particle–turbulence interactions (Elghobashi 1994, 2006). The Stokes number based on the Kolmogorov timescale τ_η is evaluated as $St_k = \tau_p/\tau_\eta$, and the variation of St_k for the particles with two densities along the wall-normal direction is presented in figure 4. According to the values of Φ_v and St_k, our simulations are located in the two-way coupled region as shown in figure 1.

https://doi.org/10.1017/jfm.2022.663 Published online by Cambridge University Press

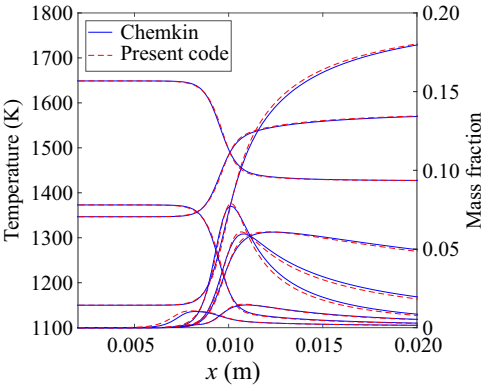


Figure 5. The temperature and species mass fraction profiles of the laminar premixed flame calculated using the present code and Chemkin.

H_2	O_2	O	OH	H_2O	H	HO_2	H_2O_2	N_2
0.32	1.15	0.75	0.76	0.84	0.19	1.16	1.16	1.0

Table 2. Lewis number for different species.

2.2. *Chemical mechanism*

In the reacting cases, a 9-species and 19-step mechanism (Li *et al.* 2004) is used for hydrogen combustion. The species diffusivities are calculated using a constant Lewis number approach, which has been widely used in combustion modeling (Hawkes & Chen 2004; Sankaran *et al.* 2007; Wang *et al.* 2021*a*). In this approach, the diffusivity of species α, i.e. D_α, can be written as $D_\alpha = D_{th}/Le_\alpha$, where D_{th} is the thermal diffusivity and Le_α is the Lewis number of species α. The Lewis numbers of different species are determined from a fit to mixture-averaged transport properties in a corresponding laminar premixed flame calculated using the software Chemkin (Kee, Rupley & Miller 1989). The resultant species Lewis numbers are provided in table 2. The preferential diffusion of species such as hydrogen is included by using different Lewis numbers for various species. The thermal diffusion, i.e. the Soret effect, is usually small compared with regular species diffusion. Therefore, it is neglected in the present work. With these treatments, the agreement between the laminar flame profiles obtained using the present code and Chemkin is excellent as seen in figure 5.

2.3. *Governing equations for the gas phase*

In the DNS, the gas phase is computed by solving the compressible transport equations for continuity, momentum, total energy and species mass fractions (Chen *et al.* 2009):

$$\frac{\partial \rho}{\partial t} = -\nabla_j \cdot (\rho u_j), \tag{2.3}$$

https://doi.org/10.1017/jfm.2022.663 Published online by Cambridge University Press

$$\frac{\partial \rho u_i}{\partial t} = -\nabla_j \cdot (\rho u_i u_j) + \nabla_j \cdot \tau_{ji} - \nabla_i p + \dot{S}_{m,i}, \tag{2.4}$$

$$\frac{\partial \rho e}{\partial t} = -\nabla_j \cdot \big(u_j(\rho e + p)\big) + \nabla_j \cdot (\tau_{ji} \cdot u_i) - \nabla_j \cdot q_j + \rho \sum_{\alpha=1}^{N_s} Y_\alpha f_{j,\alpha} \cdot (V_{j,\alpha} + u_j) + \dot{S}_e, \tag{2.5}$$

$$\frac{\partial \rho Y_\alpha}{\partial t} = -\nabla_j \cdot (\rho Y_\alpha u_j) - \nabla_j \cdot (\rho Y_\alpha V_{j,\alpha}) + \dot{\omega}_\alpha, \tag{2.6}$$

where i and j are the indices of direction for the spatial coordinate, ρ is the density, p is the pressure, τ_{ji} is the viscous stress tensor, q_j is the heat flux in direction j, Y_α is the mass fraction of species α, $\dot{\omega}_\alpha$ is the chemical source term of species α, N_s is the total number of species and $V_{j,\alpha}$ is the mass diffusion velocity for species α in the jth direction:

$$V_{j,\alpha} = -D_\alpha \frac{1}{Y_\alpha} \frac{\partial Y_\alpha}{\partial x_j}, \tag{2.7}$$

where D_α is the diffusivity of species α. The total energy e includes the internal energy and kinetic energy:

$$e = \frac{u_i u_i}{2} - \frac{p}{\rho} + \sum_{\alpha=1}^{N_s} Y_\alpha h_\alpha, \tag{2.8}$$

where h_α is the enthalpy of species α.

The spatial derivatives and time integration used an eighth-central differencing scheme and a six-stage, fourth-order explicit Runge–Kutta method, respectively (Kennedy & Carpenter 1994; Kennedy, Carpenter & Lewis 2000). High-frequency oscillations are eliminated by a tenth-order explicit spatial filter every ten time steps. The DNS advanced for more than 6τ and the stationary statistics are collected in the last 3τ, where τ is the flow-through time defined as $\tau = L_x/U_\infty$.

2.4. *Governing equations for the solid phase*

The Eulerian–Lagrangian point particle method is employed for the solid phase. As the particle volume fraction Φ_v is large enough to modulate turbulence ($10^{-6} < \Phi_v < 10^{-3}$), the two-way coupled method is considered. The effects of particles on the velocity and temperature fields of surrounding fluid are included. The source terms for the momentum, $\dot{S}_{m,i}$, and total energy, $\dot{S}_e$, are computed as

$$\dot{S}_{m,i} = -\sum_{n=1}^{n_p} \frac{m_p}{V_m} \frac{\mathrm{d}u_{p,i}^n}{\mathrm{d}t} S(\boldsymbol{x}^m, \boldsymbol{x}_p^n), \tag{2.9}$$

$$\dot{S}_e = -\sum_{n=1}^{n_p} \frac{m_p}{V_m} \frac{\mathrm{d}}{\mathrm{d}t}\left(c_{p,p} T_p^n + \frac{u_{p,i}^n u_{p,i}^n}{2}\right) S(\boldsymbol{x}^m, \boldsymbol{x}_p^n), \tag{2.10}$$

where V_m is the volume of the Cartesian grid cell which contains n_p particles, $c_{p,p}$ is the specific heat capacity of the particle, T_p^n is the temperature of the nth particle and $u_{p,i}^n$ is the velocity of the nth particle in the ith direction. The distribution coefficient $S(\boldsymbol{x}^m, \boldsymbol{x}_p^n)$

https://doi.org/10.1017/jfm.2022.663 Published online by Cambridge University Press

allocates the source terms of the nth particle on the mth grid using a smoothing kernel extrapolation approach (Capecelatro & Desjardins 2013):

$$S(\boldsymbol{x}^m, \boldsymbol{x}_p^n) = A\left(\frac{|\boldsymbol{x}^m - \boldsymbol{x}_p^n|}{9\Delta x^2} - 1\right)^4, \tag{2.11}$$

where A is a constant to ensure mass conservation, i.e. $\sum_{m=1}^{n_g} A(|\boldsymbol{x}^m - \boldsymbol{x}_p^n|/9\Delta x^2 - 1)^4 = 1$, where n_g is the number of Eulerian grids which are influenced by the nth particle. A cut-off length of $3\Delta x$ is used to avoid the particle effects in the far field. Our choice of the cut-off length is consistent with Borghesi, Mastorakos & Cant (2013) and Wang *et al.* (2021*b*). Note that removing the spurious self-induced particle disturbance is not accounted for in this approach, which might influence the accuracy of the simulations (Gualtieri *et al.* 2015; Battista *et al.* 2019). Further improvement of the coupling approach is required, which will be investigated in our future work.

The governing equations of the Lagrangian equation of particles can be expressed as

$$\frac{\mathrm{d}\boldsymbol{x}_p}{\mathrm{d}t} = \boldsymbol{u}_p, \tag{2.12}$$

$$m_p \frac{\mathrm{d}\boldsymbol{u}_p}{\mathrm{d}t} = \boldsymbol{F}_p, \tag{2.13}$$

$$c_{p,p} m_p \frac{\mathrm{d}T_p}{\mathrm{d}t} = Q_p, \tag{2.14}$$

where $\boldsymbol{x}_p$, $\boldsymbol{u}_p$ and T_p are the position vector, velocity vector and temperature of the particle, respectively, m_p is the particle mass $m_p = \pi\rho_p d_p^3/6$, and $\boldsymbol{F}_p$ and Q_p are the force and heat transfer rate, respectively. The total force acting on a particle consists of Stokes drag, lift force and thermophoretic force. As the size of the particle is smaller than the Kolmogorov length scale and the magnitude for particle-to-fluid density ratio is of $O(10^3)$, the Stokes drag is dominant (Armenio & Fiorotto 2001; Balachandar & Eaton 2010). Due to the strong shear of the boundary layer flow, the Saffman lift force can not be ignored. The thermophoretic force is also considered due to the dramatic temperature rise caused by combustion. Therefore, the force is written as

$$\boldsymbol{F}_p = \boldsymbol{F}_D + \boldsymbol{F}_{LS} + \boldsymbol{F}_T, \tag{2.15}$$

where the drag force $\boldsymbol{F}_D$ is calculated based on the drag correlation by Schiller & Naumann (1935):

$$\boldsymbol{F}_D = 3\pi\mu d_p(1 + 0.15Re_p^{0.687})(\boldsymbol{u}_f - \boldsymbol{u}_p), \tag{2.16}$$

where μ is the dynamic viscosity of the fluid and the particle Reynolds number Re_p is defined as

$$Re_p = \frac{d_p|\boldsymbol{u}_f - \boldsymbol{u}_p|}{\nu}, \tag{2.17}$$

where ν is the kinematic viscosity of the fluid.

https://doi.org/10.1017/jfm.2022.663 Published online by Cambridge University Press

The Saffman lift force is given by

$$\boldsymbol{F}_{LS} = \frac{1.615 d_p^2 \sqrt{\rho_f \mu}}{\sqrt{|\boldsymbol{\omega}|/2}} \left((\boldsymbol{u}_f - \boldsymbol{u}_p) \times \boldsymbol{\omega}/2\right) f(Re_p, Re_s), \tag{2.18}$$

where $\boldsymbol{\omega}$ is the fluid vorticity vector and expressed as

$$\boldsymbol{\omega} = \nabla \times \boldsymbol{u}_f. \tag{2.19}$$

The function $f(Re_p, Re_s)$ was first proposed by Saffman (1965, 1968) and a modified version by Mei (1992) is used in this study:

$$f(Re_p, Re_s) = \begin{cases} (1 - 0.3314\sqrt{\xi}) \exp\left(-\dfrac{Re_p}{10}\right) + 0.3314\sqrt{\xi}, & Re_p \leq 40 \\ 0.0524\sqrt{\xi Re_p}, & Re_p > 40, \end{cases} \tag{2.20}$$

where ξ is computed by $\xi = 0.5 Re_s / Re_p$ and Re_s is the shear Reynolds number,

$$Re_s = \frac{|\boldsymbol{\omega}| d_p^2}{2\nu}. \tag{2.21}$$

A data-fitting equation of thermophoretic force was proposed by James (1962) and Brock (1967):

$$\boldsymbol{F}_T = -\frac{12\pi\mu\nu R C_s \left(\dfrac{\lambda_f}{\lambda_p} + C_t \dfrac{k}{R}\right) \dfrac{\nabla T}{T_0}}{\left(1 + 3C_m \dfrac{k}{R}\right)\left(1 + 2\dfrac{\lambda_f}{\lambda_p} + 2C_t \dfrac{k}{R}\right)}, \tag{2.22}$$

where $C_m = 1.149$, $C_s = 1.13$ and $C_t = 2.17$ are the coefficients of the velocity jump, thermal creep and temperature jump, respectively, λ_f and λ_p are the thermal conductivity of the fluid and particle, respectively, with $\lambda_f = \lambda_p = 0.6$ W m^{-1} K^{-1}, R is the ideal gas constant and k is the molecular mean free path in the fluid defined as $k = KT_0/(\sqrt{2}\pi d_p^2 p_0)$, where T_0 and p_0 are the mean temperature and pressure around the particle, respectively.

The heat transfer rate Q_p is computed as

$$Q_p = \frac{Nu\, c_{p,f} m_p}{3Pr} \frac{T - T_p}{\tau_p}, \tag{2.23}$$

where $c_{p,f}$ is the fluid specific heat capacity, T is the gas temperature at the particle position, Nu is the Nusselt number and Pr is the Prandtl number (Wang *et al.* 2021*b*). The particle Biot number is less than 0.1 in all cases. Therefore, the temperature is assumed to be uniform inside the particles.

The particle equations are advanced using a six-stage, fourth-order explicit Runge–Kutta method. A fourth-order Lagrange interpolating polynomial scheme is applied to determine the fluid properties at the particle position. The Eulerian–Lagrangian point particle method has been validated in our previous work (Wang *et al.* 2020, 2021*b*). It was reported that the wall-normal distributions of the relative particle number density and the relative streamwise velocity between the fluid and particles were in a good agreement with the results by Sardina *et al.* (2012*a*) and Li *et al.* (2016*b*).

https://doi.org/10.1017/jfm.2022.663 Published online by Cambridge University Press

3. Results and discussion

In this section, first, the general characteristics of the particle-laden turbulent boundary layer flows are presented, and the heat transfer behaviours are examined. Then, the behaviours of particle wall-accumulation are explored. Finally, the effects of combustion and particles on turbulence are reported.

3.1. *General characteristics*

Figures 6 and 7 show the instantaneous distributions of temperature and streamwise velocity in a typical x–y plane for all cases, respectively. The points indicate the particle locations in a spanwise slab near the x–y plane. To highlight the temperature difference between the particles and fluid, the points are coloured by particle temperatures in figure 6. The black dashed lines in the reacting cases indicate the isosurface of the progress variable $c = 0.7$, where c is defined as

$$c = \frac{Y_{H_2} - Y_{H_{2,u}}}{Y_{H_{2,b}} - Y_{H_{2,u}}}, \tag{3.1}$$

where $Y_{H_{2,u}}$ and $Y_{H_{2,b}}$ are the H_2 mass fraction of the reactant and the product, respectively. The flow in the free stream is basically laminar, so that the flame front appears flat. In the near-wall region the flame front interacts with the boundary layer turbulence and is rather wrinkled. Note that the turbulent boundary layer is dominated by hairpin vortex structures. The turbulence level in the region between two hairpin vortices is low. The results of figures 6 and 7 are exacted from a time instant when the flame is in the region of weak turbulence and appears flat down to $y = 2$ mm. However, at other time instants, the flame might appear wrinkled up to a larger wall-normal distance (see figure 2). Several observations can be made from figure 6. First, in cases R1–R3, gas-phase temperature dramatically increases and particle temperature also increases in the product side. Second, the temperature difference between particles and their surrounding fluid is large in cases R2 and R3 with $St = 10$, whereas the difference is small in case R1 with $St = 1$. Note that the thermal lag between particles and their surrounding fluid can be characterised by the particle temperature relaxation timescale τ_T, which is proportional to τ_p as

$$\tau_T = \frac{3}{2}\frac{c_{p,p}}{c_{p,f}} Pr \tau_p, \tag{3.2}$$

where $Pr = 0.7$ is the Prandtl number. The particle relaxation time is larger for cases R2 and R3 than that for case R1, thus the thermal lag is more evident. Finally, the temperature of the product in case R3 is lower than that in cases R1 and R2. Owing to the two-way coupled effects between the particles and flow, the temperature field of the flow is modified, particularly in the DNS cases with heavy particles and large mass loadings, which further influences the heat transfer with wall. This deserves further investigation, and will be discussed in § 3.2.

Figure 7 shows the instantaneous contour of streamwise velocity and the particle locations. It is seen that the particle concentration is lower in the product side of the reacting cases than that of the non-reacting cases, which is due to the fact that combustion-induced dilatation accelerates the fluid and particles, reducing the particle concentration. Figure 7 also shows that the scales of particles disperse are larger in the cases with $St = 10$ than those in the cases with $St = 1$, which is consistent with previous studies (Lee & Lee 2015). It is also indicated that more particles tend to accumulate in the near-wall regions for the cases with $St = 10$, which will be quantified in § 3.3.

https://doi.org/10.1017/jfm.2022.663 Published online by Cambridge University Press

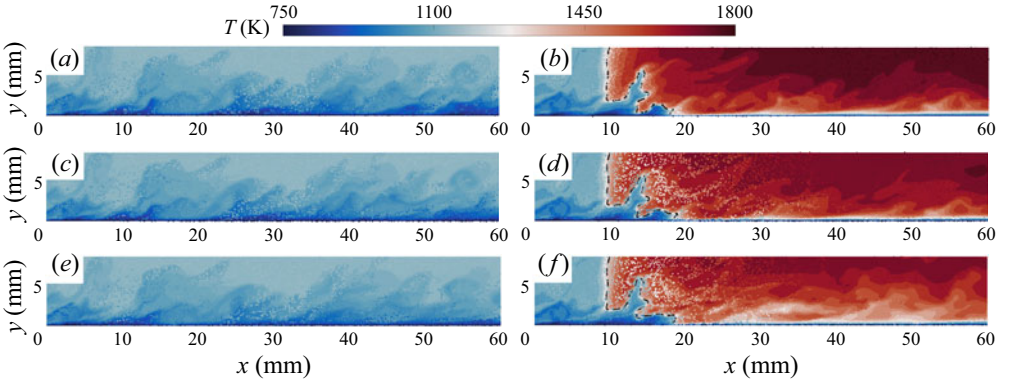


Figure 6. Instantaneous distributions of temperature of fluid and particles in a typical x–y plane for cases (a,c,e) NR1–NR3 and (b,d,f) R1–R3. The points indicate particle locations and are coloured with particle temperatures.

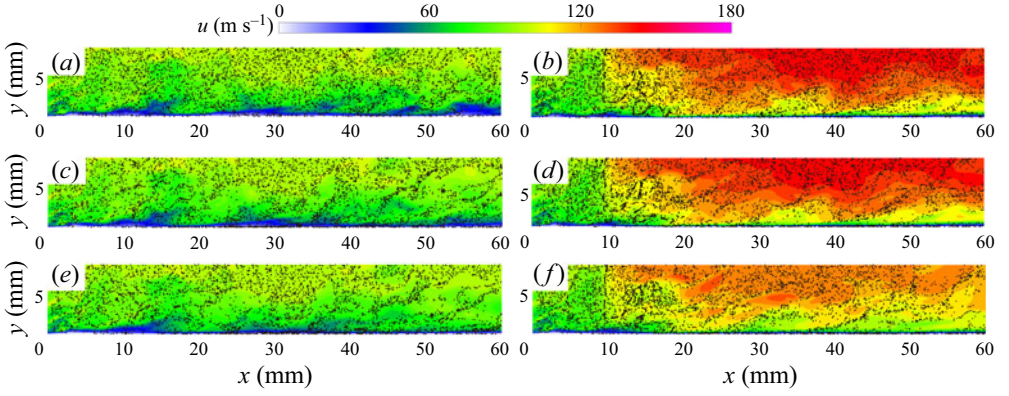


Figure 7. Instantaneous distributions of streamwise velocity of fluid in a typical x–y plane for cases (a,c,e) NR1–NR3 and (b,d,f) R1–R3. The black points indicate particle locations.

It would be interesting to examine the flame brush thickness δ_b for cases R1–R3. Here, the flame brush thickness is determined from the Favre-averaged progress variable $\tilde{c}$, which is defined as $\tilde{c} = \overline{\rho c}/\bar{\rho}$, where $\overline{(.)}$ indicates the ensemble average in the spanwise direction and in time. Figure 8 shows the distributions of $\tilde{c}$ for the reacting cases. The isolines of $\tilde{c} = 0.1$, 0.7 and 0.9 are also superimposed. Note that $\tilde{c} = 0.7$ represents the mean flame front. The flame brush thickness is defined as the distance between $\tilde{c} = 0.1$ and 0.9, which is perpendicular to the mean flame front, as illustrated in figure 8(a). The profiles of flame brush thickness as a function of the wall-normal distance for cases R1–R3 are shown in figure 8(b). It is seen that for all cases, the flame brush thickness increases with increasing wall-normal distance until $y = 4.5$ mm, and then it decreases. The flame brush thickness of case R3 is slightly smaller than those of the other two cases, which might be due to the weaker turbulence in case R3 as is discussed in more detail in § 3.3.

3.2. *Heat transfer*

The temperature distributions for the reacting cases in figure 6 imply that the gas-phase temperature of case R3 is lower compared with those of cases R1 and R2. Therefore, the

https://doi.org/10.1017/jfm.2022.663 Published online by Cambridge University Press

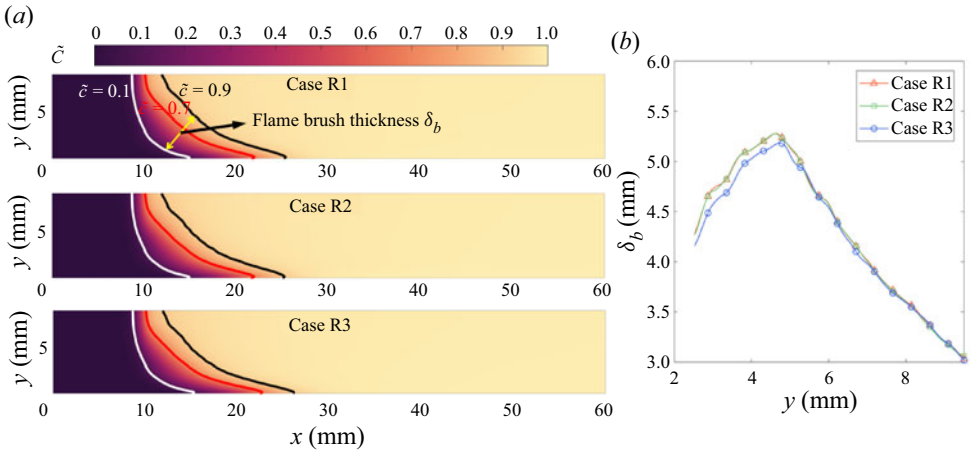


Figure 8. (*a*) The distributions of mean progress variable for the reacting cases. The isolines of $\tilde{c} = 0.1$, 0.7 and 0.9 are superimposed. (*b*) The evolution of flame brush thickness along the wall-normal direction for the reacting cases.

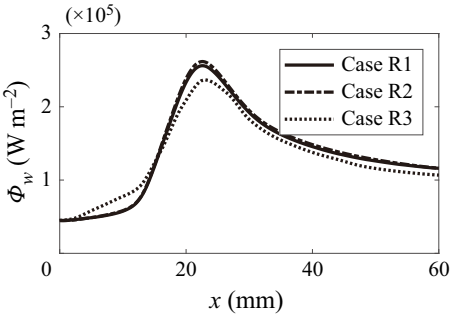


Figure 9. Evolution of mean wall heat flux for reacting cases R1–R3.

heat loss towards the wall in case R3 should be lower as the temperature difference between the gas phase and the wall is smaller. This is counterintuitive and we expect a lower heat loss to the wall would result in a higher fluid temperature as the heat release from combustion is roughly the same for all reacting cases. In this subsection, the characteristics of heat transfer are explored to explain this behaviour.

Figure 9 displays the evolution of mean wall heat flux along the streamwise direction for the reacting cases. The wall heat flux is defined as $\Phi_w = -\lambda_f \partial T/\partial y$. It is shown that, for all the reacting cases, the wall heat flux increases with x before reaching its peak around $x = 22$ mm, where the flame quenches at the wall; then the wall heat flux decreases with x. Overall, the wall heat flux for case R3 is smaller than cases R1 and R2, which indicates the heat loss to the wall is not the reason for the lower fluid temperature of case R3.

It is also noted from figure 9 that wall heat flux is higher in front of the reaction region ($x < 15$ mm) for case R3. Note that the wall heat flux is related to the wall-normal gradient of temperature in the near-wall region. Figure 10 shows the wall-normal distribution of the mean fluid temperature at $x = 10$ mm for the three reacting cases. It can be seen that the temperature of the fluid near the wall is higher in case R3 than in cases R1 and R2, whereas the temperature of the cold wall is constant (750 K). The temperature gradient along the wall-normal direction is therefore larger in case R3, and the wall heat flux is higher in case

https://doi.org/10.1017/jfm.2022.663 Published online by Cambridge University Press

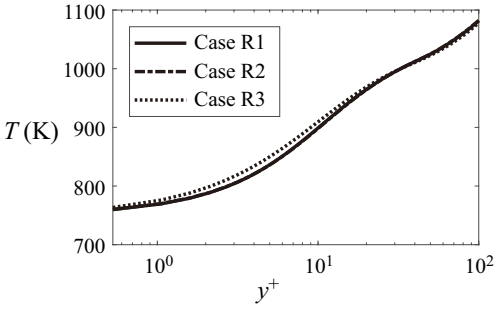


Figure 10. Wall-normal distributions of the fluid mean temperature at a streamwise location with $x = 10$ mm for reacting cases R1–R3.

R3 at $x = 10$ mm. This is due to the fact that particles with large density transfer more heat from the outer region into the near-wall region, increasing the fluid temperature. The particle mass loading for case R3 is the largest and more heat is transferred from the outer region to the near-wall region by particles, which leads to the increase of wall heat flux before $x = 15$ mm. However, the wall heat flux before $x = 15$ mm only contributes little to the total wall heat flux, which is not the main reason for the lower fluid temperature of case R3. Next, we investigate the heat transfer between the fluid and particles.

Figure 11 shows the mean distributions of particle heat transfer at the height of boundary layer thickness, i.e. $y = \delta$, along the streamwise direction. The particle heat transfer is defined as

$$\Phi_p = \frac{\sum_{i=1}^{n_p} c_{p,p}\rho_p V_{par}\dfrac{\mathrm{d}T_p^i}{\mathrm{d}t}}{\Delta x \Delta y L_z}, \tag{3.3}$$

where n_p is the number of particles in the control volume at a streamwise location. As can be seen from figure 11, the particle heat transfer increases with increasing x before reaching its peak at $x = 11$–14 mm. Notably, the value of particle heat transfer is prominent in case R3. Therefore, the heat loss from fluid to particles is the largest in case R3, and the temperature of the fluid is low in this case. It is also found that the position of the peak of Q_p in case R1 is $x = 11$ mm, whereas that in cases R2 and R3 is $x = 14$ mm. Figure 12 illustrates the distributions of mean particle temperature at the height of δ along streamwise direction for the reacting cases. The mean particle temperature increases with increasing x in the product side for the three reacting cases. Comparing various cases, it can be seen that the temperature of light particles increases faster in case R1, where the particle thermal inertia is lower.

Overall, the analysis of heat transfer indicates that the particle heat transfer is dominant over wall heat transfer in case R3. In particular, the wall heat loss of this case is the lowest among the three reacting cases. However, the heat loss to particles is the largest so that the fluid temperature of case R3 is the lowest.

3.3. *Behaviours of particles accumulation*

In this section, the behaviours of particle accumulation are explored. To quantify the particle accumulation effect, the concept of Shannon entropy is introduced (Picano *et al.* 2009), which was originally used in statistical mechanics and information theory. The Shannon entropy is analogous to the entropy in statistical thermodynamics and Shannon's

https://doi.org/10.1017/jfm.2022.663 Published online by Cambridge University Press

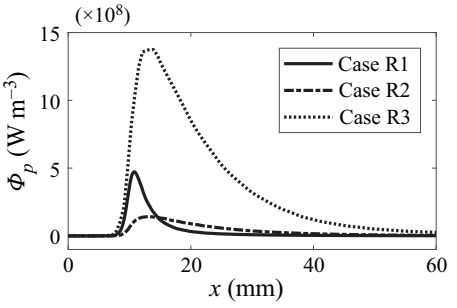


Figure 11. Mean distribution of heat transfer from fluid to particles at the height of boundary layer thickness $y = \delta$ along streamwise direction for reacting cases R1–R3.

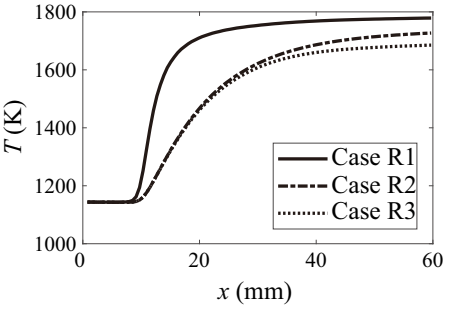


Figure 12. Mean distributions particle temperature at the height of boundary layer thickness $y = \delta$ along the streamwise direction for reacting cases R1–R3.

formula for entropy is formally identical to the Gibbs formula, which can be written as

$$H(x) = -\sum_{i=1}^{N_{sd}} P_i(x) \ln P_i(x), \tag{3.4}$$

where $P_i(x) = N_i(x)/N_t(x)$ is the probability that a particle falls in a wall-normal subdomain i. Here $N_i(x)$ and $N_t(x)$ are the averaged number of particles in the subdomain and total number in a streamwise location, respectively. The wall-normal direction within the height of boundary layer thickness δ is equally divided into $N_{sd} = 100$ subdomains. The size of each subdomain is $\Delta x \times \delta/N_{sd} \times L_z$. The flow beyond the height of δ is close to laminar, where the particles are homogeneously distributed. Therefore, only the regions within the boundary layer thickness are concerned. The entropy is normalised by its maximum among all possible distributions, which is the homogeneous distribution $H_{hom} = \ln P_{hom}$, where the homogeneous probability P_{hom} is $1/N_{sd}$. The normalised Shannon entropy $S(x) = H(x)/H_{hom}$ ranges from 0 to 1. When $S(x) = 0$, the particles concentrate in a single subdomain; when $S(x) = 1$, the particles are homogeneously distributed in the wall-normal direction.

Figure 13 shows the mean distribution of normalised Shannon entropy along the streamwise direction. As can be seen, the values of entropy near the inlet are unity for all cases, which indicates the particles have a uniform distribution initially. Several observations can be made from figure 13. First, for the non-reacting case with light particles (case NR1), the entropy is close to unity at all streamwise locations, which corresponds to a near-uniform distribution for particles. For the reacting case with light

https://doi.org/10.1017/jfm.2022.663 Published online by Cambridge University Press

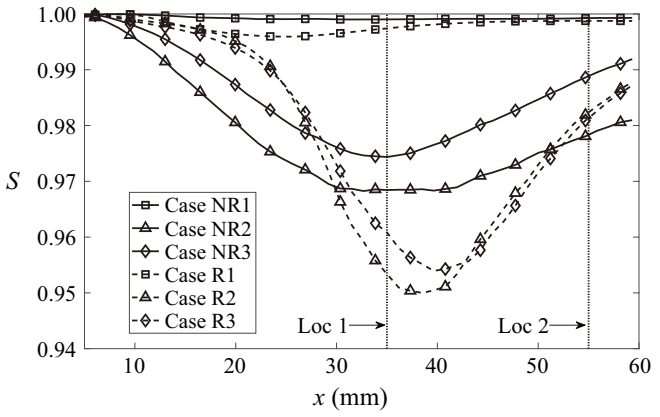


Figure 13. Mean distribution of Shannon entropy as a function of streamwise direction x.

particles (case R1), the entropy slightly decreases to its minimum around $x = 22$ mm in the flame region and recovers to unity further downstream. Second, for the cases with heavy particles (cases NR2, NR3, R2 and R3), the entropy decreases to its minimum, which corresponds to the most inhomogeneous distribution, and then increases with x. Third, the entropy is higher for the cases with a large mass loading (cases NR3 and R3) than those for the cases with a small mass loading (cases NR2 and R2), which means the distribution is more homogeneous in the cases with large mass loadings. Finally, the minimum values of entropy for the reacting cases (cases R2 and R3) are smaller than those for the non-reacting cases (cases NR2 and NR3), which means the particle distributions are more inhomogeneous for the reacting cases. The entropy for the cases with heavy particles has a minimum value around Loc1 ($x_{Loc1} = 35$ mm) and then its value increases until Loc2 ($x_{Loc2} = 55$ mm).

The entropy reflects the homogeneity of particles distribution. However, it does not provide information about the specific regions where particles accumulate. This information, as displayed in figure 14, is provided by the profiles of particle number density as a function of wall-normal direction at different streamwise locations. As can be seen, overall the particle number density decrease monotonously with y^+ and particles accumulate in the near-wall region, which indicates the inhomogeneity of particles distribution. Comparing particle number density for various cases, it is noticed the values of $N_p/N_{p,max}$ are higher at $y^+ > 50$ for the cases with light particles (cases NR1 and R1), the particle distribution of which is more homogeneous with a near-unity value of Shannon entropy as shown in figure 13. Similar observations were made by Picano *et al.* (2009) and Sardina *et al.* (2012*a*). For the reacting case R1, the value of $N_p/N_{p,max}$ beyond $y^+ = 50$ is smaller than the non-reacting case NR1. The streamwise acceleration of fluid in the flame region increases with wall-normal distance. Therefore, particles tend to move faster due to intense reactions, leading to an increased inhomogeneity of particle distribution and a reduction in entropy.

It is also noted in figure 13 that the entropy for the cases with heavy particles (cases NR2, R2, NR3 and R3) decreases to its minimum around Loc1, which corresponds to the most inhomogeneous distribution of particle number density, as shown in the yellow lines in figure 14. Comparing the non-reacting cases with different mass loadings, i.e. NR2 and NR3, $N_p/N_{p,max}$ of case NR3 is slightly larger beyond a wall-normal distance of $y^+ = 50$, which corresponds to a more homogeneous particles distribution as confirmed in figure 13.

https://doi.org/10.1017/jfm.2022.663 Published online by Cambridge University Press

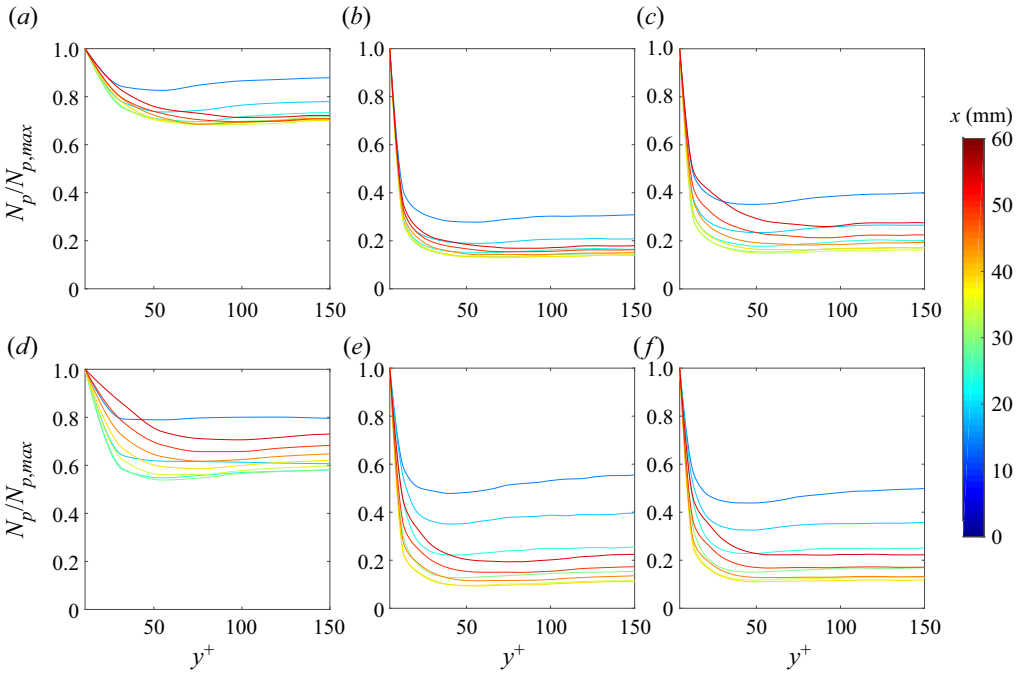


Figure 14. Wall-normal profiles of the particle number density at different streamwise locations for cases (*a–c*) NR1–NR3 and (*d–f*) R1–R3.

Particle accumulation near the wall is related to the movement of near-wall turbulence structure, which is featured by quasi-streamwise coherent vortical structures (Kaftori *et al.* 1995; Pan & Banerjee 1996; Rouson & Eaton 2001; Marchioli & Soldati 2002; Li *et al.* 2016*a*; Xiao *et al.* 2020). Figure 15 displays the instantaneous contours of streamwise vorticity at Loc2 of $x = 55$ mm, which shows that the streamwise vortices throw heavy particles out of their core and many particles accumulate in the near-wall region. The quasi-streamwise coherent vortices are responsible for the four-quadrant events in the sublayer region (Willmarth & Lu 1972), i.e. Q1 ($u' > 0$, $v' > 0$), Q2 ($u' < 0$, $v' > 0$), Q3 ($u' < 0$, $v' < 0$), Q4 ($u' > 0$, $v' < 0$), where u' is the streamwise fluctuation velocity and v' is the wall-normal fluctuation velocity. Previous studies reported that the Q2 (ejection) and Q4 (sweep) events are the dominant events in the near-wall region, which are responsible for the particle segregation and deposition. The process of particle accumulation in the near-wall region is a consequence of turbophoresis (Marchioli & Soldati 2002). To further investigate the specific regions where particles segregate and deposit, figure 16 shows a top view of instantaneous contours of fluid streamwise fluctuation velocity u' and particles in a typical buffer layer plane ($y^+ = 15$). The white and black points indicate the particles moving outward ($V_p > 0$) and inward ($V_p < 0$) to the wall, respectively. Here V_p is the instantaneous particle wall-normal velocity. The high- and low-speed streaks are clearly observed for all cases. It is noted that most particles with $V_p > 0$ tend to segregate in the low-speed streaks, which is consistent with the findings in (Uijttewaal & Oliemans 1996). Although the ejection events throw particles away from the wall, the process is much slower than that of the inward sweep events (McLaughlin 1989). Therefore, the residence time of ejection is very long in the viscous sublayer for particles, and many particles are trapped in the low-speed streaks. Combining the above results, a schematic

https://doi.org/10.1017/jfm.2022.663 Published online by Cambridge University Press

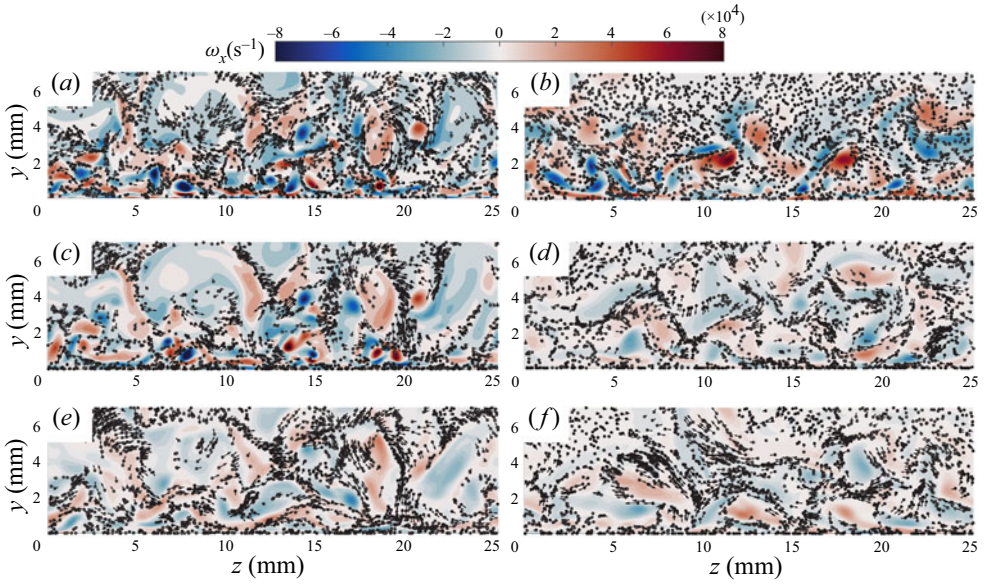


Figure 15. Instantaneous distributions of streamwise vorticity for cases (*a*,*c*,*e*) NR1–NR3 and (*b*,*d*,*f*) R1–R3 at $x = 5.5$ mm plane. The arrows indicate vectors of particle velocity.

of turbophoresis, which illustrates the process of particles segregation and deposition by quasi-streamwise coherent vortical structures, is summarised in figure 17.

Comparing the magnitude of streamwise vorticity for the non-reacting cases with heavy particles in a downstream region (Loc2), as shown in figure 15(*c*,*e*), it is noticed that the quasi-streamwise vortical structures are attenuated due to the presence of particles. The attenuation increases with increasing mass loadings. Similar observations were made by (Lee & Lee 2015; Zhou *et al.* 2020). Furthermore, the width of high- and low-speed streaks are wider in the cases with larger mass loadings as shown in figure 16. Schematics of the cases with $St = 10$ and different mass loadings are illustrated in figure 18. Overall, the scales of streamwise vortices are larger and fewer particles tend to segregate in the low-speed streaks by streamwise vortices with increasing mass loadings.

To quantify the behaviour of the quasi-streamwise vortices, the magnitude of streamwise vorticity Ω_x along the wall-normal direction is examined. The statistics are extracted from two streamwise locations, i.e. Loc1 and Loc2. Figure 19 shows the wall-normal profiles of streamwise vorticity magnitude for the cases with $St = 10$. The phenomenon of particle segregation is weakened due to the attenuation of quasi-streamwise vortices, which results in an increased entropy at Loc2. In particular, the reduction of Ω_x is prominent in case NR3, which leads to a more homogeneous particles distribution and a larger value of entropy with respect to case NR2 as shown in figure 13.

For the reacting cases, the quasi-streamwise vortices are also attenuated by combustion as shown in figures 15 and 16. Turbulence is attenuated and the width of high- and low-speed streaks is increased for all reacting cases in downstream regions. As shown in figure 19, the values of Ω_x are smaller for the reacting cases than the corresponding non-reacting cases at Loc2. Therefore, for the reacting cases, the turbophoresis effects are reduced, and the particles distribution is more uniform at Loc2. At Loc1, fluid streamwise acceleration induced by combustion increases with increasing y^+, resulting

https://doi.org/10.1017/jfm.2022.663 Published online by Cambridge University Press

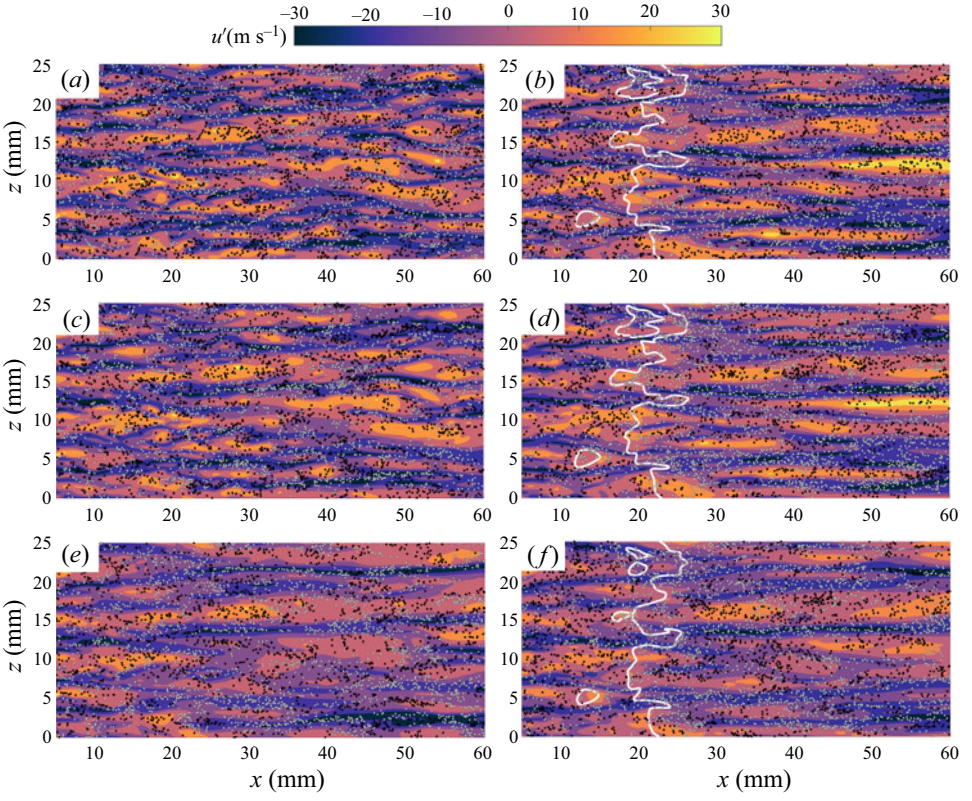


Figure 16. Top view of instantaneous distributions of fluctuation of streamwise velocity u' with particles for cases (*a*,*c*,*e*) NR1–NR3 and (*b*,*d*,*f*) R1–R3 in a typical buffer layer plane ($y^+ = 15$). The white lines in the reacting cases indicate the isosurfaces of progress variable $c = 0.7$. The points are coloured by the motions of particles (outward, $V_p > 0$, and inward, $V_p < 0$, are coloured by white and black, respectively).

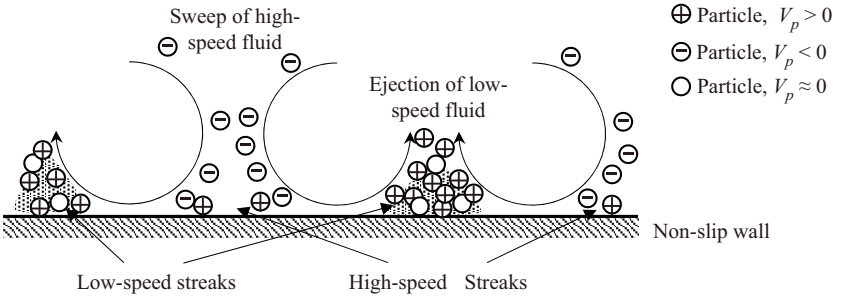


Figure 17. Schematics of the turbophoresis process of heavy particles segregation and deposition by quasi-streamwise vortices.

in a more inhomogeneous particles distribution and a reduction of entropy compared with the corresponding non-reacting cases.

https://doi.org/10.1017/jfm.2022.663 Published online by Cambridge University Press

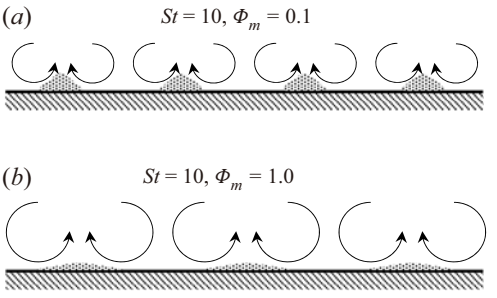


Figure 18. Schematics of interactions between heavy particles ($St = 10$) and quasi-streamwise vortices for cases with (*a*) $\Phi_{m,in} = 0.1$ and (*b*) $\Phi_{m,in} = 1.0$.

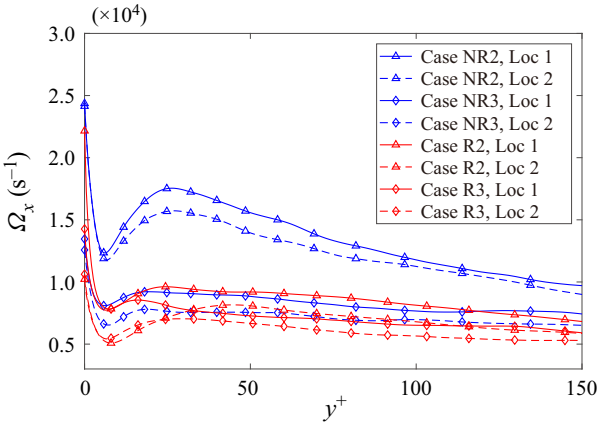


Figure 19. The magnitude of streamwise vorticity as a function of wall-normal distance y^+ for cases with heavy particles in Loc1 and Loc2.

3.4. *Turbulence modulation*

The near-wall turbulence is modulated by combustion and particles. To investigate the effects of combustion and particles on turbulent boundary layer flows, the flow topologies and the anisotropy of the Reynolds stress are examined in this subsection.

3.4.1. *Flow topology*

The local flow topologies are characterised by the velocity gradient tensor $\boldsymbol{A}$:

$$A_{ij} = \frac{\partial u_i}{\partial x_j} = S_{ij} + W_{ij}, \tag{3.5}$$

where $S_{ij} = (A_{ij} + A_{ji})/2$ and $W_{ij} = (A_{ij} - A_{ji})/2$ are the tensors of strain rate and rotation, respectively.

The quantities λ_1, λ_2 and λ_3 are the three principal eigenvalues of S_{ij}, with the convention $\lambda_1 \geq \lambda_2 \geq \lambda_3$, which are the solution of the following characteristic equation:

$$\lambda^3 + P\lambda^2 + Q\lambda + R = 0, \tag{3.6}$$

https://doi.org/10.1017/jfm.2022.663 Published online by Cambridge University Press

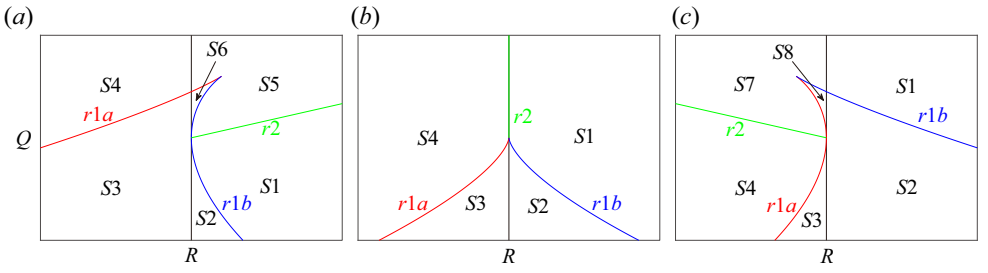


Figure 20. The topological classifications in the Q–R plane with the lines $r1a$, $r1b$ and $r2$ dividing the topologies for (a) $P < 0$, (b) $P = 0$ and (c) $P < 0$.

	Acronym	Description
S1	FC/U	Foci/Compressing, Unstable
S2	NSS/U	Node/Saddle/Saddle, Unstable
S3	NSS/S	Node/Saddle/Saddle, Stable
S4	FS/S	Foci/Stretching, Stable
S5	FC/S	Foci/Comprssing, Stable
S6	NNN/S	Node/Node/Node, Stable
S7	FS/U	Foci/Stretching, Unstable
S8	NNN/U	Node/Node/Node, Unstable

Table 3. Classification of flow topology types.

where P, Q and R are the tensor invariants and specified as

$$P = -\mathrm{tr}(\boldsymbol{A}) = -S_{ii}, \tag{3.7}$$

$$Q = \tfrac{1}{2}\left([\mathrm{tr}(\boldsymbol{A})]^2 - \mathrm{tr}(\boldsymbol{A}^2)\right) = \tfrac{1}{2}(P^2 - S_{ij}S_{ji} - W_{ij}W_{ji}) \quad \text{and} \tag{3.8}$$

$$R = -\det(\boldsymbol{A}) = \tfrac{1}{3}(-P^3 + 3PQ - S_{ij}S_{jk}S_{ki} - 3W_{ij}W_{jk}S_{ki}). \tag{3.9}$$

For compressible flows, eight topological classifications can be identified in P–Q–R space, which are simplified from the 27 topologies reported by Chong, Perry & Cantwell (1990). A schematic of these flow topologies is displayed in figure 20. The classification of the different topologies and their acronyms are given in table 3, which can be categorised as strain-dominant nodal types (S2, S3, S6 and S8) and vortex-dominant foci types (S1, S4, S5 and S7). The P–Q–R space is split by the following lines:

$$r1a: \quad \tfrac{1}{3}P\left(Q - \tfrac{2}{9}P^2\right) - \tfrac{2}{27}(-3Q + P^2)^{3/2} - R = 0, \tag{3.10}$$

$$r1b: \quad \tfrac{1}{3}P\left(Q - \tfrac{2}{9}P^2\right) + \tfrac{2}{27}(-3Q + P^2)^{3/2} - R = 0, \tag{3.11}$$

$$r2: \quad PQ - R = 0. \tag{3.12}$$

Figure 21 shows the probability density function (p.d.f.) of P, Q and R at Loc2 for various cases. The results from three representative wall-normal locations, i.e. $y^+ = 5$ (viscous sublayer), $y^+ = 30$ (buffer) and $y^+ = 120$ (logarithmic layer), are displayed in solid, dashed and dotted lines, respectively. The results of the non-reacting and reacting cases are represented in blue and red lines, respectively. The three invariants P, Q and

https://doi.org/10.1017/jfm.2022.663 Published online by Cambridge University Press

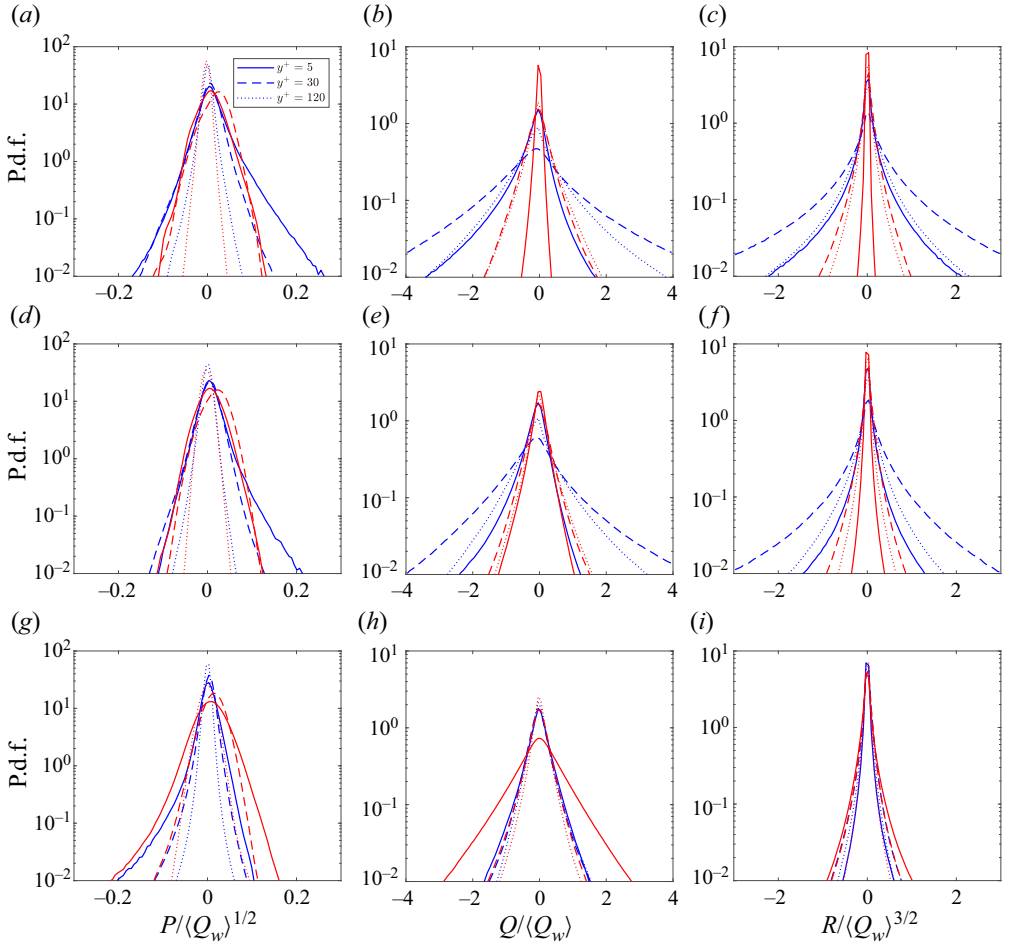


Figure 21. Probability density function of three normalised invariants: P, Q and R at three wall normal locations for cases (*a–c*) NR1 and R1, (*d–f*) NR2 and R2 and (*g–i*) NR3 and R3 at Loc2. The blue and red lines represent the results of non-reacting and reacting cases, respectively. The solid, dashed and dotted lines indicate the results at the height of $y^+ = 5$ (viscous sublayer), $y^+ = 30$ (buffer layer) and $y^+ = 120$ (logarithmic layer).

R are respectively normalised by $\langle Q_w\rangle^{1/2}$, $\langle Q_w\rangle$ and $\langle Q_w\rangle^{3/2}$, where $\langle Q_w\rangle$ is the mean of $Q_w = -W_{ij}W_{ji}/2$. The average is performed inside the boundary layer and in time for case NR1. As shown in figure 21, the p.d.f.s of P in the near-wall regions ($y^+ = 5$ and $y^+ = 30$) are wider than that in the logarithmic layer ($y^+ = 120$). This is because the flows in the near-wall regions can be compressed by the cold wall, and can be expanded by inward sweeping particles that come from the outer region with higher temperature. The mean values of P in the near-wall regions are positive for all cases, which means that the fluid compression is dominant in this region. It is also found, in the cases with $\Phi_{m,in} = 0.1$, the p.d.f. of Q and R is the broadest in the buffer layer, the second broadest in the logarithmic layer, and the narrowest in viscous sublayer. In contrast, in the cases with $\Phi_{m,in} = 1.0$, the p.d.f. of Q and R is the broadest in the viscous sublayer. Similar observations were reported in a previous study of an incompressible particle-laden turbulent boundary layer by Bijlard *et al.* (2010).

https://doi.org/10.1017/jfm.2022.663 Published online by Cambridge University Press

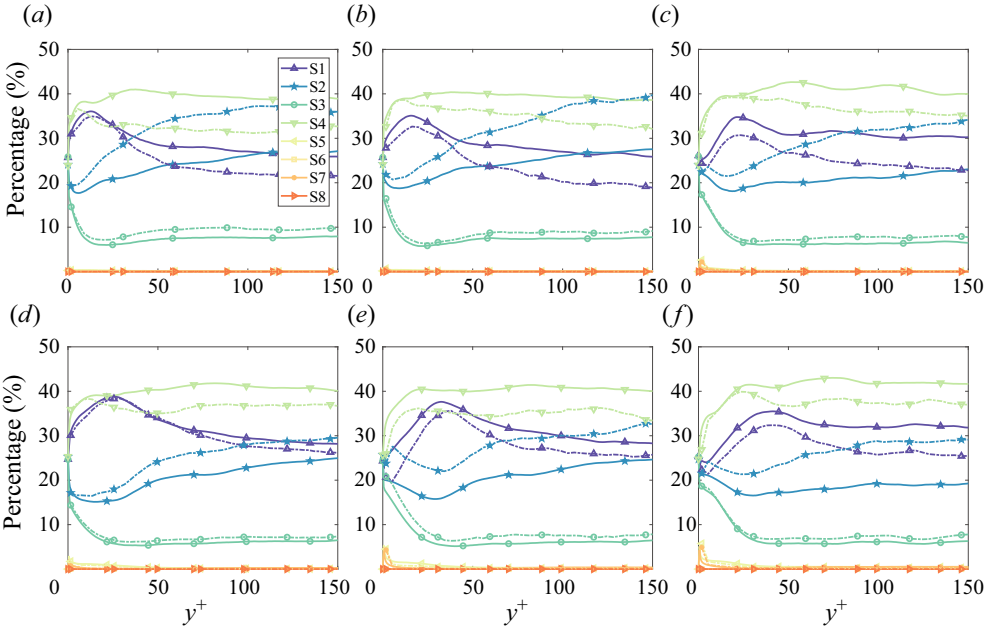


Figure 22. The percentages of flow topologies of fluid field for cases (*a*,*c*,*e*) NR1–NR3 and (*b*,*d*,*f*) R1–R3. The solid and dashed lines indicate the volume fractions of flow topologies sampled on the Eulerian grids and sampled on particle locations, respectively.

Figure 22 shows the profiles of volume fractions of flow topologies sampled on the Eulerian grids and sampled on particle locations, which are indicated by solid and dashed lines, respectively. It is observed the vortex-dominant nodal regions (S1 and S4) dominate the strain-dominant focal regions (S2 and S3). The volume fraction of S4 generally increases as y^+ increases, and dominates in the logarithmic layer. For cases NR1 and NR2, the second most probable topology is S1 in the viscous sublayer and buffer layer, and the volume fraction of S2 surpasses S1 in the logarithmic layer. As for case NR3 and the three reacting cases, the second, third and fourth most probable topologies are S1, S2 and S3, respectively, across the boundary layer. The volume fractions of S5–S8 are low due to the low compressibility of the flow in the present study.

Figure 22 shows the percentages of the vortex-dominant nodal topologies (S1 and S4) sampled on particle locations are lower than those sampled on Eulerian grids, whereas the percentages for strain-dominant focal topologies (S2 and S3) are higher when sampled on particle locations. This indicates that particles tend to accumulate at strain-dominant topologies (S2 and S3), and tend to run way from vortex-dominant topologies (S1 and S4) for all cases.

Comparing the results of the cases with different Stokes numbers, it can be seen that the volume fraction of vortex-dominant topologies (S1 and S4) in the near-wall region ($y^+ < 30$) is higher for the cases with $St = 1$ than the cases with $St = 10$, whereas the volume fraction of strain-dominant topologies (S2 and S3) is lower for the cases with $St = 1$ than the cases with $St = 10$. This further confirms that heavy particles favours strain-dominant topologies in the near-wall region.

3.4.2. *Anisotropy of the Reynolds stress*

To better understand the effects of combustion and particles on turbulence structures, the anisotropy of the Reynolds stress is explored. The normalised Reynolds-stress anisotropy

https://doi.org/10.1017/jfm.2022.663 Published online by Cambridge University Press

tensor b_{ij} is defined as (Lumley & Newman 1977)

$$b_{ij} = \frac{R_{ij}}{R_{kk}} - \frac{1}{3}\delta_{ij}, \tag{3.13}$$

where $R_{ij} = \overline{u_i' u_j'}$ is the Reynolds stress. Here σ_1, σ_2 and σ_3 are the three eigenvalues of this tensor, which are the solution of the following characteristic equation:

$$\sigma^3 - I_b\sigma^2 + II_b\sigma - III_b = 0, \tag{3.14}$$

where I_b, II_b and III_b are the three invariants for the anisotropy tensor and given as

$$I_b = b_{kk} = 0, \quad II_b = -b_{ij}b_{ji}, \quad III_b = b_{ij}b_{jk}b_{ki}. \tag{3.15a–c}$$

The joint trajectories of the second and third invariants along the wall-normal direction are enclosed by the curvilinear triangle, i.e. the 'Lumley triangle' as shown in figure 23, which was introduced by Lumley & Newman (1977). The expressions of the boundary for the Lumley triangle are given as

$$\text{left}: \quad -II_b = 3\left(\tfrac{1}{4}III_b^2\right)^{1/3}, \quad (III_b < 0), \tag{3.16}$$

$$\text{right}: \quad -II_b = 3\left(\tfrac{1}{4}III_b^2\right)^{1/3}, \quad (III_b > 0), \tag{3.17}$$

$$\text{top}: \quad -II_b = 3III_b + \tfrac{1}{9}. \tag{3.18}$$

The left and right boundaries of the triangle correspond to the disc-like and rod-like turbulence, respectively, whereas the top straight line corresponds to the two-dimensional turbulence. The bottom ($III_b = 0$), left ($III_b < 0$) and right ($III_b > 0$) vertices of the triangle correspond to three-dimensional isotropic, two-dimensional isotropic and one-component turbulence, respectively.

Figure 23 illustrates the anisotropy invariant mapping for different cases at Loc2. The squares and circles represent the joint trajectories of II_b–III_b based on the fluid and particle velocity, respectively. Several trends are observed. First, for cases NR1 and NR2, the trajectories of the flow in the viscous sublayer lie on the top straight line, indicating the high- and low-speed streaks are roughly 2-D structures. The trajectories for the motions of particles approach 1-D structure in the viscous sublayer, which is more prominent in the cases with $St = 10$. Second, as the wall-normal distance increases, the trajectories of the flow travel along the top line, and then change their direction to rod-like turbulence in the buffer layer, where the flow tends to be long vortex tubes. Finally, as the trajectories in the logarithmic layer approach the origin of the coordinate, the flow becomes more isotropic.

To reveal the effect of combustion on turbulence, the trajectories in the non-reacting (figure 23*a*,*c*,*e*) and reacting (figure 23*b*,*d*,*f*) cases are compared. It is observed that, in the reacting cases, the trajectories approach 1-D structure more closely. Remember that the streaks are longer for the reacting cases (figure 16), which is consistent with the fact that the structure of the flow is more 1-D in the reacting cases. To explore the effects of mass loading on turbulence, the trajectories for the cases with $\Phi_{m,in} = 0.1$ (figure 23*c*,*d*) and the cases with $\Phi_{m,in} = 1.0$ (figure 23*e*,*f*) are compared. As can be seen, the trajectories approach to 1-D structure more closely in the cases with a large mass loading, corresponding to the longer streaky structures in the buffer layer (see figure 16).

https://doi.org/10.1017/jfm.2022.663 Published online by Cambridge University Press

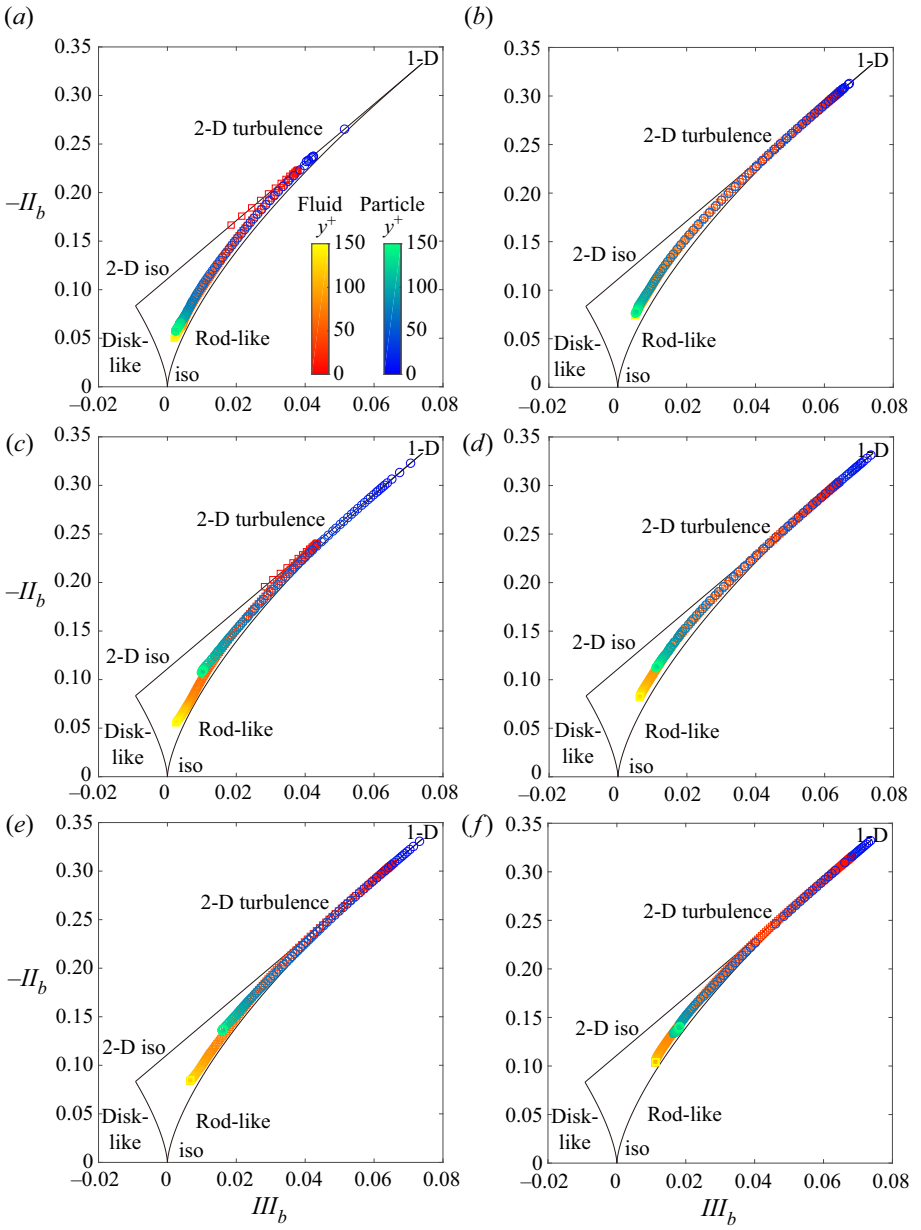


Figure 23. Anisotropy invariant mapping (Lumley triangle) of the turbulent stress for cases at Loc2 (*a*,*c*,*e*) NR1–NR3 and (*b*,*d*,*f*) R1–R3, where the horizontal and vertical axes denote the third and second invariants, respectively.

4. Conclusion

In the present study, turbulent particle-laden boundary layer flows with and without combustion have been investigated using DNS. The point particle method has been employed for the solid phase in the Lagrangian framework, whereas the flow has been solved in an Eulerian way. In the reacting cases, a 9-species and 19-step mechanism for hydrogen combustion has been used. The complex interactions of boundary layer

https://doi.org/10.1017/jfm.2022.663 Published online by Cambridge University Press

turbulence, combustion and particles in the configuration have been examined from the perspective of heat transfer, particle accumulation and turbulence modulation. The main conclusions are summarised as follows.

The general characteristics of the particle-laden turbulent boundary layer flows have been explored. It has been found that, in the reacting cases, the flame brush thickness is smaller in the case with heavy particles and a large mass loading (case R3), which might be due to the lower turbulent intensity. In addition, it has been observed that the temperature of the product in case R3 is lower than that in case R1 and R2. The heat transfer characteristics have been studied, showing that the wall heat flux (particle heat transfer) for case R3 is the lowest (highest). It was, therefore, concluded that the particle heat transfer is dominant over wall heat transfer and results in a lower fluid temperature for case R3.

The particle accumulation in the near-wall region has been investigated via Shannon entropy analysis, which reflects the homogeneity of particle distribution along the wall-normal direction. Compared with light particles, more heavy particles segregate in the near-wall region. The particles move faster with increasing wall-normal distance due to combustion, which results in more inhomogeneous distribution in the reacting cases. The quasi-streamwise coherent vortices determine the four-quadrant events in the sublayer region, among which the sweep and ejection events are responsible for the particle wall-accumulation (i.e. the turbophoresis effect). The magnitude of streamwise vorticity is suppressed by heavy particles, and the suppression increases with increasing mass loadings, which results in a more homogeneous particle distribution for the case with a large mass loading than that with a small mass loading.

The flow topologies and the anisotropy of Reynolds stress have been explored to study the boundary layer turbulence modulation by combustion and particles. It has been observed that light particles favour the vortex-dominant topologies, whereas heavy particles favour the strain-dominant topologies. The anisotropy analysis shows that the near-wall flow becomes more one-dimensional due to combustion and increasing mass loadings, which corresponds to the longer streaky structures in the near-wall region.

In our future work, reacting particles will be included to understand the particle ignition process and examine the effects of reacting particles on boundary layer turbulence.

Funding. This work was supported by Natural Science Foundation of China (Grant Nos. 51836007 and 52022091).

Declaration of interests. The authors report no conflict of interest.

Author ORCIDs.
Haiou Wang https://orcid.org/0000-0002-6480-2657;
Jianren Fan https://orcid.org/0000-0002-6332-6441.

References

Alshaalan, T. & Rutland, C.J. 2002 Wall heat flux in turbulent premixed reacting flow. *Combust. Sci. Technol.* **174**, 135–165.

Armenio, V. & Fiorotto, V. 2001 The importance of the forces acting on particles in turbulent flows. *Phys. Fluids* **13**, 2437–2440.

Balachandar, S. & Eaton, J.K. 2010 Turbulent dispersed multiphase flow. *Annu. Rev. Fluid Mech.* **42**, 111–133.

Battista, F., Mollicone, J.-P., Gualtieri, P., Messina, R. & Casciola, C.M. 2019 Exact regularised point particle (erpp) method for particle-laden wall-bounded flows in the two-way coupling regime. *J. Fluid Mech.* **878**, 420–444.

https://doi.org/10.1017/jfm.2022.663 Published online by Cambridge University Press

BATTISTA, F., PICANO, F., TROIANI, G. & CASCIOLA, C.M. 2011 Intermittent features of inertial particle distributions in turbulent premixed flames. *Phys. Fluids* **23**, 123304.

BIJLARD, M.J., OLIEMANS, R.V.A., PORTELA, L.M. & OOMS, G. 2010 Direct numerical simulation analysis of local flow topology in a particle-laden turbulent channel flow. *J. Fluid Mech.* **653**, 35–56.

BORGHESI, G., MASTORAKOS, E. & CANT, R.S. 2013 Complex chemistry DNS of n-heptane spray autoignition at high pressure and intermediate temperature conditions. *Combust. Flame* **160**, 1254–1275.

BROCK, J.R. 1967 The thermal force in the transition region. *J. Colloid Interface Sci.* **23** (3), 448–452.

BROOKE, J.W., HANRATTY, T.J. & MCLAUGHLIN, J.B. 1994 Free-flight mixing and deposition of aerosols. *Phys. Fluids* **6**, 3404–3415.

BRUNEAUX, G., AKSELVOLL, K., POINSOT, T. & FERZIGER, J.H. 1996 Flame-wall interaction simulation in a turbulent channel flow. *Combust. Flame* **107**, 27–36.

BRUNEAUX, G., POINSOT, T. & FERZIGER, J.H. 1997 Premixed flame–wall interaction in a turbulent channel flow : budget for the flame surface density evolution equation and modelling. *J. Fluid Mech.* **349**, 191–219.

CAPECELATRO, J. & DESJARDINS, O. 2013 An Euler–Lagrange strategy for simulating particle-laden flows. *J. Comput. Phys.* **238**, 1–31.

CAPECELATRO, J., DESJARDINS, O. & FOX, R.O. 2016 Strongly coupled fluid-particle flows in vertical channels. I. Reynolds-averaged two-phase turbulence statistics. *Phys. Fluids* **28**, 033306.

CAPECELATRO, J., DESJARDINS, O. & FOX, R.O. 2018 On the transition between turbulence regimes in particle-laden channel flows. *J. Fluid Mech.* **845**, 499–519.

CHEN, J.H., *et al.* 2009 Terascale direct numerical simulations of turbulent combustion using S3D. *Comput. Sci. Disc.* **2**, 015001.

CHEN, G., WANG, H., LUO, K. & FAN, J. 2021 Flame edge structures and dynamics in planar turbulent non-premixed inclined slot-jet flames impinging at a wall. *J. Fluid Mech.* **920**, A43.

CHONG, M.S., PERRY, A.E. & CANTWELL, B.J. 1990 A general classification of three-dimensional flow fields. *Phys. Fluids* A **2**, 765–777.

COSTA, P., BRANDT, L. & PICANO, F. 2020 Interface-resolved simulations of small inertial particles in turbulent channel flow. *J. Fluid Mech.* **883**, A54.

COSTA, P., BRANDT, L. & PICANO, F. 2021 Near-wall turbulence modulation by small inertial particles. *J. Fluid Mech.* **922**, A9.

CROWE, C.T. 2000 On models for turbulence modulation in fluid–particle flows. *Intl J. Multiphase Flow* **26**, 719–727.

DREIZLER, A. & BÖHM, B. 2015 Advanced laser diagnostics for an improved understanding of premixed flame–wall interactions. *Proc. Combust. Inst.* **35**, 37–64.

DRISCOLL, J.F., CHEN, J.H., SKIBA, A.W., CARTER, C.D., HAWKES, E.R. & WANG, H. 2020 Premixed flames subjected to extreme turbulence: some questions and recent answers. *Prog. Energy Combust. Sci.* **76**, 100802.

DRITSELIS, C.D. & VLACHOS, N.S. 2008 Numerical study of educed coherent structures in the near-wall region of a particle-laden channel flow. *Phys. Fluids* **20**, 55103.

DRITSELIS, C.D. & VLACHOS, N.S. 2011 Numerical investigation of momentum exchange between particles and coherent structures in low re turbulent channel flow. *Phys. Fluids* **23**, 25103.

ELGHOBASHI, S. 1994 On predicting particle-laden turbulent flows. *Appl. Sci. Res.* **52**, 309–329.

ELGHOBASHI, S. 2006 An updated classification map of particle-laden turbulent flows. In *IUTAM Symposium on Computational Approaches to Multiphase Flow* (ed. S. Balachandar & A. Prosperetti), pp. 3–10. Springer.

ELGHOBASHI, S. & TRUESDELL, G.C. 1993 On the two-way interaction between homogeneous turbulence and dispersed solid particles. I: turbulence modification. *Phys. Fluids* A **5**, 1790–1801.

FESSLER, J.R., KULICK, J.D. & EATON, J.K. 1994 Preferential concentration of heavy particles in a turbulent channel flow. *Phys. Fluids* **6**, 3742–3749.

FOX, R.O. 2014 On multiphase turbulence models for collisional fluid–particle flows. *J. Fluid Mech.* **742**, 368–424.

GANAPATHISUBRAMANI, B., CLEMENS, N.T. & DOLLING, D.S. 2006 Large-scale motions in a supersonic turbulent boundary layer. *J. Fluid Mech.* **556**, 271–282.

GORE, R.A. & CROWE, C.T. 1989 Effect of particle size on modulating turbulent intensity. *Intl J. Multiphase Flow* **15**, 279–285.

GRUBER, A., SANKARAN, R., HAWKES, E.R. & CHEN, J.H. 2010 Turbulent flame–wall interaction: a direct numerical simulation study. *J. Fluid Mech.* **658**, 5–32.

GUALTIERI, P., PICANO, F., SARDINA, G. & CASCIOLA, C.M. 2015 Exact regularized point particle method for multiphase flows in the two-way coupling regime. *J. Fluid Mech.* **773**, 520–561.

https://doi.org/10.1017/jfm.2022.663 Published online by Cambridge University Press

HAWKES, E.R. & CHEN, J.H. 2004 Direct numerical simulation of hydrogen-enriched lean premixed methane–air flames. *Combust. Flame* **138**, 242–258.

HETSRONI, G., MOSYAK, A. & POGREBNYAK, E. 2002 Effect of coarse particles on the heat transfer in a particle-laden turbulent boundary layer. *Intl J. Multiphase Flow* **28**, 1873–1894.

JAMES, R.B. 1962 On the theory of thermal forces acting on aerosol particles. *J. Colloid Sci.* **17**, 768–780.

KAFTORI, D., HETSRONI, G. & BANERJEE, S. 1995 Particle behavior in the turbulent boundary layer. I. Motion, deposition, and entrainment. *Phys. Fluids* **7**, 1095–1106.

KEE, R.J., RUPLEY, F.M. & MILLER, J.A. 1989 *Chemkin-II: A Fortran chemical kinetics package for the analysis of gas-phase chemical kinetics* (No. SAND-89-8009). Sandia National Lab. (SNL-CA).

KENNEDY, C.A. & CARPENTER, M.H. 1994 Several new numerical methods for compressible shear-layer simulations. *Appl. Numer. Maths* **14**, 397–433.

KENNEDY, C.A., CARPENTER, M.H. & LEWIS, R.M. 2000 Low-storage, explicit Runge–Kutta schemes for the compressible Navier–Stokes equations. *Appl. Numer. Maths* **35**, 177–219.

KUERTEN, J.G.M. 2016 Point-particle DNS and LES of particle-laden turbulent flow – a state-of-the-art review. *Flow Turbul. Combust.* **97**, 689–713.

KUERTEN, J.G.M., VAN DER GELD, C.W.M. & GEURTS, B.J. 2011 Turbulence modification and heat transfer enhancement by inertial particles in turbulent channel flow. *Phys. Fluids* **23**, 123301.

KULICK, J.D., FESSLER, J.R. & EATON, J.K. 1994 Particle response and turbulence modification in fully developed channel flow. *J. Fluid Mech.* **277**, 109–134.

LEE, J. & LEE, C. 2015 Modification of particle-laden near-wall turbulence: effect of Stokes number. *Phys. Fluids* **27**, 23303.

LI, D., LUO, K. & FAN, J. 2016*a* Modulation of turbulence by dispersed solid particles in a spatially developing flat-plate boundary layer. *J. Fluid Mech.* **802**, 359–394.

LI, D., LUO, K. & FAN, J. 2018 Direct numerical simulation of turbulent flow and heat transfer in a spatially developing turbulent boundary layer laden with particles. *J. Fluid Mech.* **845**, 417–461.

LI, Y., MCLAUGHLIN, J.B., KONTOMARIS, K. & PORTELA, L. 2001 Numerical simulation of particle-laden turbulent channel flow. *Phys. Fluids* **13**, 2957–2967.

LI, D., WEI, A., LUO, K. & FAN, J. 2016*b* Direct numerical simulation of a particle-laden flow in a flat plate boundary layer. *Intl J. Multiphase Flow* **79**, 124–143.

LI, J., ZHAO, Z., KAZAKOV, A. & DRYER, F.L. 2004 An updated comprehensive kinetic model of hydrogen combustion. *Intl J. Chem. Kinet.* **36**, 566–575.

LIPATNIKOV, A.N. & CHOMIAK, J. 2010 Effects of premixed flames on turbulence and turbulent scalar transport. *Prog. Energy Combust. Sci.* **36**, 1–102.

LUMLEY, J.L. & NEWMAN, G.R. 1977 The return to isotropy of homogeneous turbulence. *J. Fluid Mech.* **82**, 161–178.

MARCHIOLI, C. & SOLDATI, A. 2002 Mechanisms for particle transfer and segregation in a turbulent boundary layer. *J. Fluid Mech.* **468**, 283–315.

MCLAUGHLIN, J.B. 1989 Aerosol particle deposition in numerically simulated channel flow. *Phys. Fluids* A **1**, 1211–1224.

MEI, R. 1992 An approximate expression for the shear lift force on a spherical particle at finite Reynolds number. *Intl J. Multiphase Flow* **18**, 145–147.

MILLER, R.S. & BELLAN, J. 1999 Direct numerical simulation of a confined three-dimensional gas mixing layer with one evaporating hydrocarbon-droplet-laden stream. *J. Fluid Mech.* **384**, 293–338.

MOSER, R.D., KIM, J. & MANSOUR, N.N. 1999 Direct numerical simulation of turbulent channel flow up to $Re_\tau = 590$. *Phys. Fluids* **11**, 943–945.

NAKHAEI, M. & LESSANI, B. 2017 Effects of solid inertial particles on the velocity and temperature statistics of wall bounded turbulent flow. *Intl J. Heat Mass Transfer* **106**, 1014–1024.

NARAYANAN, C., LAKEHAL, D., BOTTO, L. & SOLDATI, A. 2003 Mechanisms of particle deposition in a fully developed turbulent open channel flow. *Phys. Fluids* **15**, 763–775.

NASR, H., AHMADI, G. & MCLAUGHLIN, J.B. 2009 A DNS study of effects of particle–particle collisions and two-way coupling on particle deposition and phasic fluctuations. *J. Fluid Mech.* **640**, 507–536.

NIÑO, Y. & GARCIA, M.H. 1996 Experiments on particle—turbulence interactions in the near–wall region of an open channel flow: implications for sediment transport. *J. Fluid Mech.* **326**, 285–319.

NILSEN, C., ANDERSSON, H.I. & ZHAO, L. 2013 A Voronoï analysis of preferential concentration in a vertical channel flow. *Phys. Fluids* **25**, 115108.

PAN, Y. & BANERJEE, S. 1996 Numerical simulation of particle interactions with wall turbulence. *Phys. Fluids* **8**, 2733–2755.

PEDINOTTI, S., MARIOTTI, G. & BANERJEE, S. 1992 Direct numerical simulation of particle behaviour in the wall region of turbulent flows in horizontal channels. *Intl J. Multiphase Flow* **18**, 927–941.

https://doi.org/10.1017/jfm.2022.663 Published online by Cambridge University Press

PICANO, F., BATTISTA, F., TROIANI, G. & CASCIOLA, C.M. 2011 Dynamics of PIV seeding particles in turbulent premixed flames. *Exp. Fluids* **50**, 75–88.

PICANO, F., SARDINA, G. & CASCIOLA, C.M. 2009 Spatial development of particle-laden turbulent pipe flow. *Phys. Fluids* **21**, 93305.

PICCIOTTO, M., MARCHIOLI, C. & SOLDATI, A. 2005 Characterization of near-wall accumulation regions for inertial particles in turbulent boundary layers. *Phys. Fluids* **17**, 98101.

POINSOT, T.J., HAWORTH, D.C. & BRUNEAUX, G. 1993 Direct simulation and modeling of flame–wall interaction for premixed turbulent combustion. *Combust. Flame* **95**, 118–132.

PORTELA, L.M. & OLIEMANS, R.V.A. 2003 Eulerian–Lagrangian DNS/LES of particle–turbulence interactions in wall-bounded flows. *Intl J. Numer. Meth. Fluids* **43**, 1045–1065.

RASHIDI, M., HETSRONI, G. & BANERJEE, S. 1990 Particle-turbulence interaction in a boundary layer. *Intl J. Multiphase Flow* **16**, 935–949.

REEKS, M.W. 1983 The transport of discrete particles in inhomogeneous turbulence. *J. Aerosol Sci.* **14**, 729–739.

RICHTER, D.H. 2015 Turbulence modification by inertial particles and its influence on the spectral energy budget in planar Couette flow. *Phys. Fluids* **27**, 063304.

ROGERS, C.B. & EATON, J.K. 1991 The effect of small particles on fluid turbulence in a flat-plate, turbulent boundary layer in air. *Phys. Fluids* A **3**, 928–937.

ROUSON, D.W.I. & EATON, J.K. 2001 On the preferential concentration of solid particles in turbulent channel flow. *J. Fluid Mech.* **428**, 149–169.

SAFFMAN, P.G. 1965 The lift on a small sphere in a slow shear flow. *J. Fluid Mech.* **22**, 385–400.

SAFFMAN, P.G. 1968 The lift on a small sphere in a slow shear flow – corrigendum. *J. Fluid Mech.* **31**, 624–624.

SANKARAN, R., HAWKES, E.R., CHEN, J.H., LU, T. & LAW, C.K. 2007 Structure of a spatially developing turbulent lean methane–air Bunsen flame. *Proc. Combust. Inst.* **31**, 1291–1298.

SARDINA, G., SCHLATTER, P., BRANDT, L., PICANO, F. & CASCIOLA, C.M. 2012*a* Wall accumulation and spatial localization in particle-laden wall flows. *J. Fluid Mech.* **699**, 50–78.

SARDINA, G., SCHLATTER, P., PICANO, F., CASCIOLA, C.M., BRANDT, L. & HENNINGSON, D.S. 2012*b* Self-similar transport of inertial particles in a turbulent boundary layer. *J. Fluid Mech.* **706**, 584–596.

SCHILLER, L. & NAUMANN, Z.A. 1935 Drag coefficient correlation. *Z. Verein. Deutsch. Ing.* **77**, 318–320.

SCHLATTER, P. & ÖRLÜ, R. 2010 Assessment of direct numerical simulation data of turbulent boundary layers. *J. Fluid Mech.* **659**, 116–126.

SQUIRES, K.D. & EATON, J.K. 1991 Preferential concentration of particles by turbulence. *Phys. Fluids* **3**, 1169–1178.

UIJTTEWAAL, W.S.J. & OLIEMANS, R.V.A. 1996 Particle dispersion and deposition in direct numerical and large eddy simulations of vertical pipe flows. *Phys. Fluids* **8**, 2590–2604.

WANG, H., CHEN, G., LUO, K., HAWKES, E.R., CHEN, J.H. & FAN, J. 2021*a* Turbulence/flame/wall interactions in non-premixed inclined slot-jet flames impinging at a wall using direct numerical simulation. *Proc. Combust. Inst.* **38**, 2711–2720.

WANG, H., LUO, K., HAWKES, E.R., CHEN, J.H. & FAN, J. 2021*b* Turbulence, evaporation and combustion interactions in n-heptane droplets under high pressure conditions using DNS. *Combust. Flame* **225**, 417–427.

WANG, G. & RICHTER, D.H. 2019 Two mechanisms of modulation of very-large-scale motions by inertial particles in open channel flow. *J. Fluid Mech.* **868**, 538–559.

WANG, Y. & TROUVÉ, A. 2006 Direct numerical simulation of nonpremixed flame–wall interactions. *Combust. Flame* **144**, 461–475.

WANG, Z., WANG, H., LUO, K. & FAN, J. 2020 Direct numerical simulation of particle-laden turbulent boundary layers without and with combustion. *Phys. Fluids* **32**, 105108.

WANG, H., WANG, Z., LUO, K., HAWKES, E.R., CHEN, J.H. & FAN, J. 2021*c* Direct numerical simulation of turbulent boundary layer premixed combustion under auto-ignitive conditions. *Combust. Flame* **228**, 292–301.

WILLMARTH, W.W. & LU, S.S. 1972 Structure of the Reynolds stress near the wall. *J. Fluid Mech.* **55**, 65–92.

XIAO, W., JIN, T., LUO, K., DAI, Q. & FAN, J. 2020 Eulerian–Lagrangian direct numerical simulation of preferential accumulation of inertial particles in a compressible turbulent boundary layer. *J. Fluid Mech.* **903**, A19.

YOUNG, J. & LEEMING, A. 1997 A theory of particle deposition in turbulent pipe flow. *J. Fluid Mech.* **340**, 129–159.

ZHAO, L., ANDERSSON, H.I. & GILLISSEN, J.J.J. 2010 Turbulence modulation and drag reduction by spherical particles. *Phys. Fluids* **22**, 81702.

https://doi.org/10.1017/jfm.2022.663 Published online by Cambridge University Press

ZHAO, L., ANDERSSON, H.I. & GILLISSEN, J.J.J. 2013 Interphasial energy transfer and particle dissipation in particle-laden wall turbulence. *J. Fluid Mech.* **715**, 32–59.

ZHAO, P., WANG, L. & CHAKRABORTY, N. 2018 Analysis of the flame–wall interaction in premixed turbulent combustion. *J. Fluid Mech.* **848**, 193–218.

ZHOU, T., ZHAO, L., HUANG, W. & XU, C. 2020 Non-monotonic effect of mass loading on turbulence modulations in particle-laden channel flow. *Phys. Fluids* **32**, 43304.

ZONTA, F., MARCHIOLI, C. & SOLDATI, A. 2008 Direct numerical simulation of turbulent heat transfer modulation in micro-dispersed channel flow. *Acta Mech.* **195**, 305–326.

https://doi.org/10.1017/jfm.2022.663 Published online by Cambridge University Press